이학박사학위논문

Functional Structure of Correlated Cortical Activity in Human Visual Areas

인간 시각영역내 상관된 대뇌활동의 기능구조

2017 년 2 월

서울대학교 대학원

자연과학대학 뇌인지과학과

류 중 원

Abstract

Functional Structure of Correlated Cortical Activity in Human Visual Areas

Jungwon Ryu

Department of Brain and Cognitive Sciences

The Graduate School

Seoul National University

The cerebral cortex is a large-scale network, where processing units are intimately connected. In the sensory system, a sensory organ and downstream cortical regions communicate through hierarchical connections, and local sites within the regions communicate through

horizontal connections. In such interconnected networks, neural activities at local sites are likely to influence one another in complex ways and thus are intricately correlated. Recognizing the functional importance of correlated population activity in sensory representation, the neural activities arising spontaneously without the external stimuli have been studied via diverse local or global measures in various time scales. Here, measuring functional magnetic resonance imaging (fMRI) signals in human early visual cortex, we studied the structure of correlated population activity. Guided by previously known biases in anatomical connection patterns, we evaluated and compared the contributions of three relational factors to the correlated fMRI activities. Namely, all possible pairs of gray matter sites in visual areas were characterized (i) in terms of how far the receptive fields of two sites are from each other over retinotopic space, (ii) in terms of how far two sites are over cortical surface, and (iii) in terms of how similarly two sites are tuned to visual features, spatial frequency and orientation. We found that, although the three relational factors all have their own contributions in accounting for the structure of correlated fMRI activity, the tuning similarity factors overrode the distance factors. The predominance of tuning similarity was evident both within and between V1, V2, and V3, irrespective of the presence or degree of visual stimulation. We also

found that the stimulus-tuned covariability systematically varied depending on the angular positions and the eccentricity in the visual field. Moreover, we found that the pairwise covariability of spontaneous fMRI activities fluctuated dynamically over time, and that this temporal dynamics was governed by both the distance factors and the tuning similarity factors. In general, our findings suggest that the spontaneous cortical activities in the human early visual areas can be understood as the interplays among local sites constituting a multilayered network, where different layers are governed by different distance or function factors. In specific, our study demonstrated that the layers governed by the stimulus tuning similarity are far more dominant than those governed by the distance factors.

Keywords: spontaneous activity, covariance structure, resting state, functional connectivity, stimulus tuning, visual cortex, cortical travelling wave, functional magnetic resonance imaging (fMRI), cortical distance

Student Number: 2010-30767

Contents

List of Figures

1. INTRODUCTION

1.1. Correlated Population Activity in Visual Cortex

The brain recruits a large pool of neurons to perceive, interpret, and act on the environment. Indeed, neural populations spread throughout sensory, cognitive, and motor systems can act in concert, affecting various aspects of animal or human behavior, including vision (Hesselmann et al. 2008; Monto et al. 2008; Schölvinck et al. 2011), somatosensory perception (Boly et al. 2007), motor execution (Fox et al. 2007), and response time (Snyder et al. 2015; see Palva and Palva 2012 for review). Intriguingly, these concerted activities are often correlated on a large scale, exhibiting robust patterns of correlation in the absence of stimulation (Fox et al. 2005; Yeo et al. 2011), which are shaped by experiences (Lewis et al. 2009; Stevens et al. 2010; Baldassarre et al. 2012). The structure of correlated cortical activities begets diverse impacts on the amount or quality of information carried by a large sensory neuronal pool (Zohary et al. 1994; Averbeck et al. 2006). Thus,

for understanding the neural processes substantiating sensory perception, it is important to identify what relationships in sensory neural populations contribute, and with what degrees, to the structure of correlated activity.

1.2. Connectivity Structures in Visual Cortex

In the visual cortex, previous anatomical and functional imaging studies suggest three relationships between neural sites as candidate factors that potentially contribute to correlated activity (Fig. 1). First, as suggested by the existence of significant correlations in spontaneous activity among nearby sites in the retina (Meister 1996), correlated neural responses could be mediated by horizontal connections within the retina and further augmented by shared retino-cortical projections ("retinotopic distance [RD]" factor; Fig. 1*A*). Second, the degree of correlation among responses could depend on the distance between sites over the cortical surface (Das and Gilbert 1999) ("cortical distance [CD]" factor; Fig. 1*B*). Consistent with this idea, primary visual cortex (V1) neurons disperse

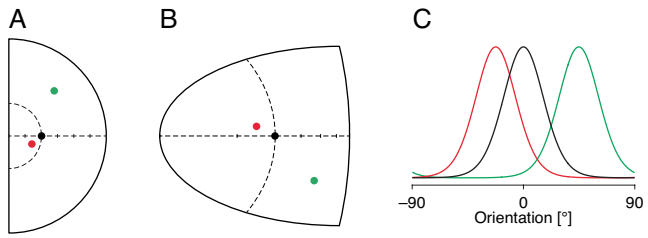

Figure 1. Three candidate relational factors for correlated variability in V1

In the example shown here, the three hypotheses offer different accounts for a higher correlation between the black (seed) and red sites than between the black and green sites. (*A*) Receptive field (RF) positions of the example sites in the right visual hemifield. The dashed half circle and horizontal line demarcate the iso-eccentricity and the iso-angular positions aligned to the seed site's RF, respectively. The small, vertical ticks on the meridian demarcate equally spaced eccentricity positions. The variance in correlated activity is regressed on the distance between the V1 site RFs defined on the retina. (*B*) Locations of the example sites, along with the lines and ticks shown in *A*, projected onto the flattened cortical surface of left-hemisphere V1. The degree of correlation between two sites is determined directly by the cortical distance between the sites. (*C*) Orientation tuning curves of the example sites. The similarity in tuning curve shape determines the degree of correlation between two sites.

their horizontal axon terminals mainly in neighboring neurons (Douglas et al. 1995). And third, correlated variability could be ascribed to a functional measure, namely, the shared visual feature tuning ("tuning similarity" factor; Fig. 1*C*), because the lateral projections in V1 preferentially exist among columns with similar tuning properties (Bosking et al. 1997; Sincich and Blasdel 2001; Stettler et al. 2002).

To date, the structure of correlated activity in the visual cortex has been mostly studied by simultaneously recording the spiking activity

of many neurons within local regions of animal brains. These studies demonstrated the contribution of tuning similarity factors by reporting systematic changes in correlated activity as a function of tuning similarity in various stimulus dimensions, including spatial and temporal frequency (Glickfeld et al. 2013), orientation (Ts'o et al. 1986; Gilbert and Wiesel 1989), ocular dominance (Malach et al. 1993), direction of motion and speed (Huang and Lisberger 2009), and color (Roe and Ts'o 1999; Chu et al. 2014). As mentioned earlier, structured patterns of correlation are also found in large-scale activities, including those measurable in human brains with functional magnetic resonance imaging (fMRI) (Fox et al. 2005). Recent fMRI studies showed that the correlations of spontaneous blood oxygenation level-dependent (BOLD) activity in human early visual areas depend on the distance factors, in retinotopic or cortical space (Heinzle et al. 2011; Butt et al. 2013; Arcaro et al. 2015). But it remains untested whether tuning similarity factors affect the large-scale correlated activity.

Aiming to answer this question, we acquired tuning similarity measures, both in spatial frequency (SF) and orientation (OR), for individual cortical site pairs in the human visual cortex using the fMRI methods established by previous studies (Henriksson et al. 2008; Freeman et al. 2011; Park et al. 2013; Choe et al. 2014). We then

examined whether and how those tuning similarity measures affected the degree to which BOLD signals are correlated between sites during the absence and presence of visual stimuli. Our results clearly indicate that, while both distance and tuning similarity factors do have their own contributions, tuning similarity governs the core architecture of correlated BOLD activity both within and between human early visual areas at diverse spatial scales, irrespective of the presence or degree of visual stimulation.

2. CORRELATED FMRI ACTIVITY TUNED TO STIMULUS FEATURE

To evaluate the contributions of the three relational factors to the correlated activity in the early visual cortex, we acquired and analyzed data as follows. First, we defined the measures for RD and CD factors and tuning similarity factors, and estimated the values of those measures, one for each, for all of the possible pairs of unit gray matter volumes (2 mm iso voxels) in the V1, V2, and V3 areas of seven human subjects. Then, we measured the pairwise correlations in spontaneous BOLD activity and inspected the relationship of those correlations with the relational factors by carrying out simple correlation, part correlation, and multiple regression analyses. To determine how the structure of correlated activity was affected by the presence of visual input, we repeated the same analyses on the BOLD time series in which the pairwise correlations were defined from moment-to-moment fluctuations within and/or between visual areas during the presentation of high contrast visual stimuli. Finally, we expanded the analyses for the correlations at larger spatial scales, between visual field quadrants and hemispheres.

2.1. Definition for Retinotopic, Cortical Distance and Tuning Similarity

We used several different metrics to define the RD factor. The primary metric was the Euclidean distance between the retinotopic positions of voxel pairs, which were estimated from retinotopic mapping scans (Figs. 2*A,B*, and 3*A*). To ensure the reliability of RD estimates, we selected voxels with high SNR and small s.d. of the time courses in the absence of visual stimuli, and discarded voxels with estimated eccentricities and angular positions that differed substantially from those of neighboring voxels (see MATERIALS AND METHODS). The resulting retinotopic position estimates were consistent between two independent subsets of scans (across-subject mean correlation coefficient [s.d.], 0.956 [0.026] for eccentricity estimation, and 0.910 [0.055] for angular position estimation; Fig. 4). Because previous studies showed that spiking activities are strongly correlated when receptive fields (RFs) overlap (Jermakowicz et al. 2009; Greschner et al. 2011), we also estimated the degree of RF overlap between voxels as an alternative metric for retinotopic proximity,

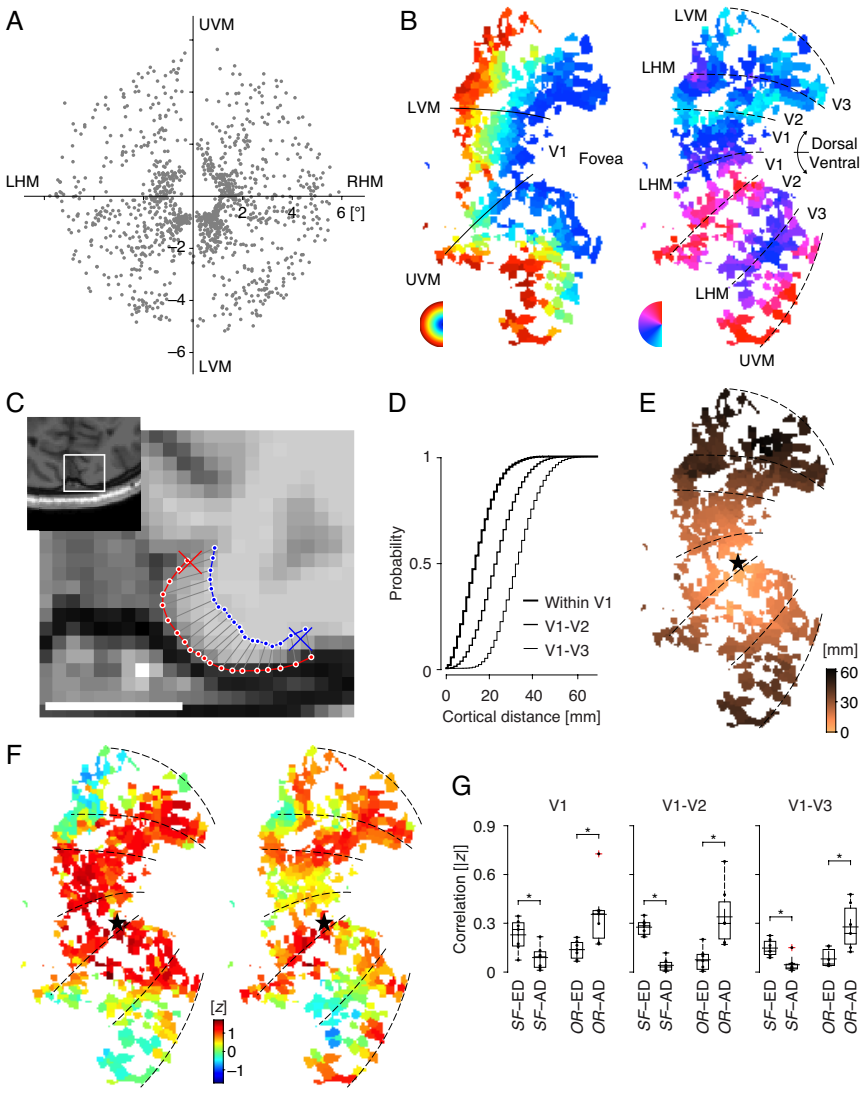

Figure 2 Metrics of the three relational factors defined for the visual cortex

(A) The dots represent the individual voxels in V1, V2, and V3 projected onto the visual field. UVM, upper vertical meridian; RHM, right horizontal meridian; LVM, lower vertical meridian; LHM, left horizontal meridian. (B) Eccentricity (left) and angular position (right) values of the voxels overlaid on the flattened surface of the right-hemisphere visual cortex. (C) Definition of cortical distance (CD)

illustrated on an axial slice of a T1-weighted anatomy image. The columns (gray lines) belonging to voxels (center positions displayed as red and blue crosses) were identified by selecting the closest pairs of white and gray matter vertices (red and blue dots, respectively). Given the highly folded geometry of the cortical surface, we validated the accuracy of CDs by searching for two independent paths, traced along the gray (red curve) and white (blue curve) matter surfaces, and used one or the average of them, depending on the cortical depth of a given voxel pair (see MATERIALS AND METHODS for details). The square in the inset is a zoomed out view. Scale bar, 10 mm. (D) Cumulative histograms of CDs. (E) CDs from a reference voxel (star). (F) Tuning similarities in spatial frequency (SF; left) and orientation (OR; right) with the reference voxel (star). (G) Population summary of the absolute correlations of SF or OR tuning similarities (SF, OR, respectively) with eccentricity or angular position differences (ED, AD, respectively). Correlations between OR and AD (OR-AD) are computed by the linear-circular correlations (Berens 2009). Dots represent individual subjects, and crosses their averages. (D,G) V1 voxel pairs were taken within the same hemisphere, while V1-V2 and V1-V3 voxel pairs were taken within dorsal or ventral regions within hemispheres. (A–F) Data from a representative subject. (G) Population data from seven subjects.

which will be described in detail below (subsection *Receptive field overlap* in ***Controls for Alternative Explanations***).

The metric for defining the CD factor was the length of the shortest path connecting two virtual cortical columns over the cortical surface (Figs. 2*C* and 3*B*). The resulting distributions of CD measures shifted from short to long distances as voxel pairs were taken from cortical areas further spatially separated (Fig. 2*D*). In addition, when projected onto the flattened cortical surface, the estimated distances

from an arbitrarily defined seed voxel exhibited roughly isotropic linear gradients (Fig. 2*E*).

The measure for defining tuning similarity was the correlation between the response profiles of two voxels to stimuli varying in SF or OR (Fig. 2*F*). The stimulus tuning of a voxel was estimated from the average profiles of the BOLD responses to visual patterns whose SF or OR changed gradually over time (Fig. 3*C,D*). Subsequently, correlations between the mean response profiles of given pairs of voxels (top and middle panels of Fig. 3*F*) were computed to estimate tuning similarity. We opted to quantify the tuning similarity in this way, rather than by computing the distance between the peaks of tuning profiles as is typically done in single-cell studies, because the tuning profiles of single voxels reflect aggregates of tuning curves of many neurons; hence, entire tuning profiles should be taken into account.

As expected, our estimates of tuning similarity exhibited the two previously known spatial biases in stimulus tuning along the polar-coordinate axes of retinotopic space (Henriksson et al. 2008; Freeman et al. 2011). When the tuning similarity was characterized in terms of SF (left panel of Fig. 2*F*; the pairwise comparisons including SF in Fig. 2*G*), it was more strongly correlated with the difference in eccentricity than

with the difference in angular position for the voxel pairs defined within V1 (t_6 = 2.893, P = 0.028; paired-sample t-test on the absolute values of correlation coefficients), for those defined between V1 and V2 (t_6 = 9.332, P < 0.001), and for those defined between V1 and V3 (t_6 = 3.574, P = 0.012). By contrast, when the tuning similarity was characterized by OR (right panel of Fig. 2*F*; the pairwise comparisons including OR in Fig. 2*G*), it was more strongly correlated with the difference in angular position than with the difference in eccentricity for the voxel pairs defined within V1 (t_6 = 2.666, P = 0.037), for those defined between V1 and V2 (t_6 = 3.111, P = 0.020), and for those defined between V1 and V3 (t_6 = 3.233, P = 0.018). The issues associated with these relationships between tuning similarity and polar-coordinate retinotopic position will be addressed in detail below with the results of the control analyses (described in ***Controls for Alternative Explanations***).

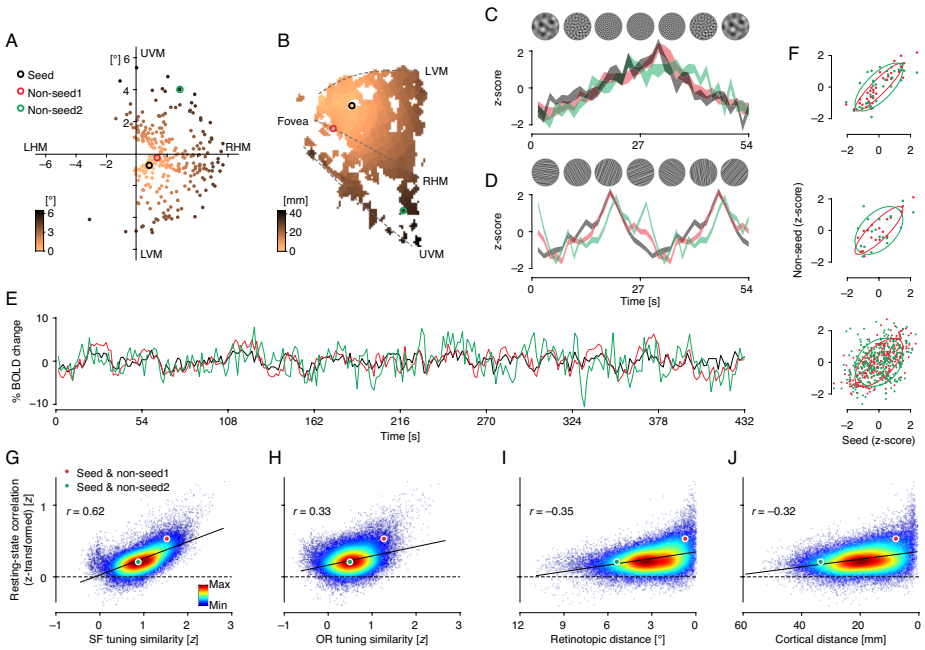

Figure 3. Relationships of resting-state correlation with three relational factors in the left-hemisphere V1 of a representative subject

(*A*–*D*) Three exemplar voxels are marked with colored circles (*A,B*) or traces (*C,D*). Retinotopic distances (RDs; *A*) and CDs (*B*) from the seed voxel are plotted as the colors at their locations on the visual field (*A*) and on the cortical surface, respectively, for all valid voxels. (*C,D*) Average time courses of fMRI responses to periodic presentations of SF and OR stimuli. Thickness of the line traces, s.e.m. across trials. (*C*) SF increases to the maximum value for the first half of the cycle (27 s) and decreases to the minimum value for the subsequent half in this example. (*D*) OR rotates clockwise in this example. For illustration, two cycles of identical time courses were concatenated. (*E*) Example time series of resting-state fMRI activity during one scan. (*F*) The average responses to SF (top) and OR stimuli (middle), and resting-state activities (bottom) of the non-seed voxel plotted against those of the seed voxels. Colors represent voxel pairs (see legend in *G*). Individual dots in top, middle, and bottom panels correspond to each time frame in *C*, *D*, and *E*, respectively. Ellipses, one standard deviation from centroids. (*G*–*I*) Density scatter plots of resting-state correlations against stimulus tuning similarities and distances. Individual dots are all possible pairs of the voxels shown in *A* and *B*, and their colors represent the normalized joint histogram of

voxel pairs. Solid lines are linear regressions of resting-state correlations on relational factors.

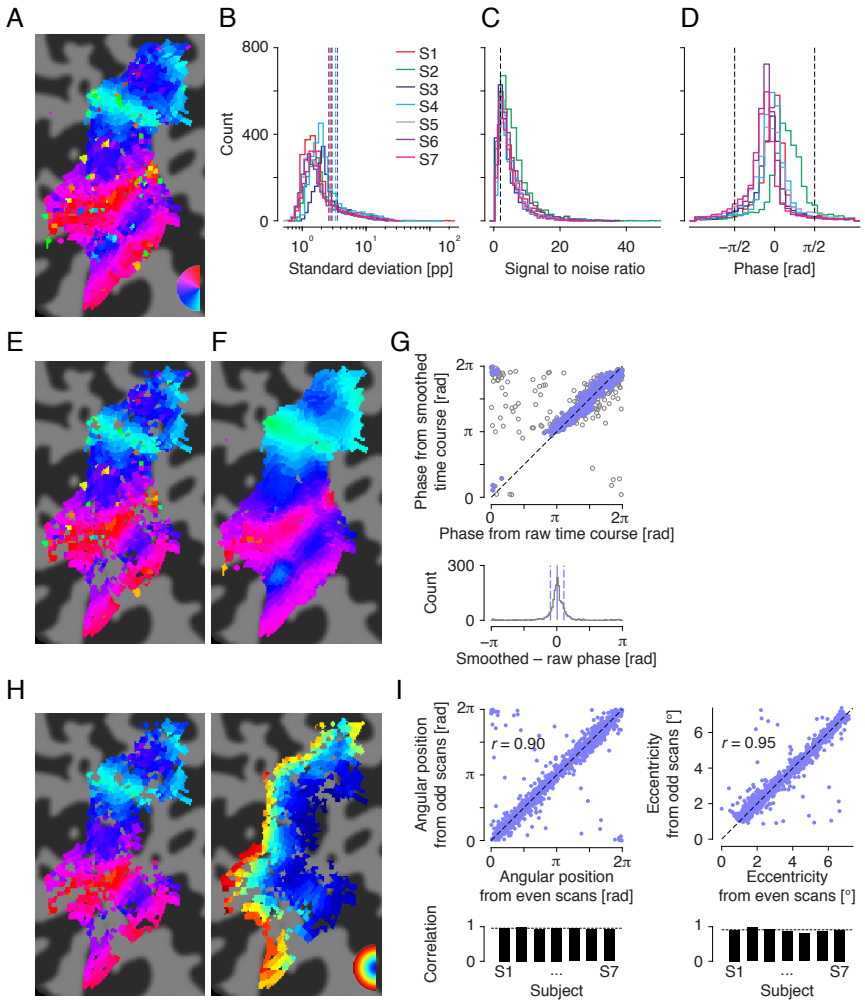

Figure 4. Procedures and criteria for selecting valid voxels

(*A*) Retinotopic angular positions of an original (before screening) set of voxels in areas V1, V2, and V3 overlaid on the flattened cortical surface of the right hemisphere of a representative subject. Refer to the inset for the color code. (*B*) Histograms (colored solid lines) of the s.d.s of percent signal changes in fMRI

activity during the resting state for the original set of voxels, including those shown in *A*. The voxels with s.d.s greater than the top 20th percentile, indicated by the colored dashed lines drawn separately for the seven individual subjects, were discarded because they are likely to reflect non-neuronal activities originating from large blood vessels. (*C*) Histograms of the signal to noise ratios (SNRs) of fMRI responses to the simple on-/off-stimulation of whole-field visual patterns for the original set of voxels, including those shown in *A*. Voxels with SNR > 2, indicated by the black dashed line, were selected as valid ones. (*D*) Histograms of the phase of sine functions fitted to the fMRI responses to the simple on-/off-stimulation of whole-field visual patterns for the original set of voxels, including those shown in *A*. The voxels with temporal phases within $\pm\pi/2$, indicated by the black dashed line, were selected as valid ones. (*E*) Retinotopic angular positions of the voxels that passed the three criteria illustrated in *B*, *C*, and *D*. The invalid voxels can be identified as the sites missing their original colors shown in *A*. (*F*) Retinotopic angular positions of the original set of voxels estimated from the spatially smoothed response time courses. For smoothing, a Gaussian filter with 0.8 mm sigma was iteratively (20 times) applied to each image frame of the original angular position mapping scans, used to generate the map shown in *A*. This filtered map of angular positions was created to be compared with *E*, allowing for detecting the voxels whose values differed substantially from their neighbors (see *G*). (*G*) Top, raw (as shown in *A*) and smoothed (as shown in *F*) phase values of voxels' time series during angular position mapping scans plotted against each other. Data from the right hemisphere as in *A*. Bottom, a histogram of angular position differences between the raw and smoothed phase values. The voxels differing by more than $\sqrt{2}$ angular deviations away from the circular mean of phase differences denoted as solid vertical line (empty circles in the top panel; outside the dashed vertical line in the bottom panel) were discarded as invalid ones. (*H*) Retinotopic angular position (left) and eccentricity (right) of the final set of voxels that passed all of the four criteria illustrated in *B*–*D* and *G*. The invalid voxels can be identified as the sites missing their original colors shown in *A*. (*I*) Correlations in angular position (left column) and eccentricity (right column) values between the even- and odd-numbered scans for the valid voxels from the representative subject shown in *A*,*E*–*H* (top row), and their population summaries (bottom row). Here, the data were from both hemispheres. The dotted lines at the bottom panels represent the means across the seven subjects who participated in the main experiment.

2.2. Stimulus-Tuned Covariability in V1, V2, and V3 During Resting State

Having defined the measures for the relational factors, we measured spontaneous BOLD activity while subjects closed their eyes, with the light from the projector physically blocked. To ensure subjects did not fall asleep, we monitored their eyelids with an infrared camera during scans and verbally communicated with them between scans. As reported previously (Bianciardi et al. 2009), spontaneous activity fluctuated and correlated strongly in the regime of low (< 0.1 Hz) temporal frequency (Fig. 5). We computed a correlation between spontaneous BOLD activities for each voxel pair, which will be referred to hereafter as the resting-state correlation (Fig. 3*E* and bottom panel in Fig. 3*F*), and then quantified the contributions of the relational factors by computing the correlations between those factors and resting-state correlations. To fulfill the linearity assumption, we transformed the correlation values into *z* values using Fisher's *z* transformation (Fig. 3*G–J*; for detailed information and results without transformations, see Fig. 11).

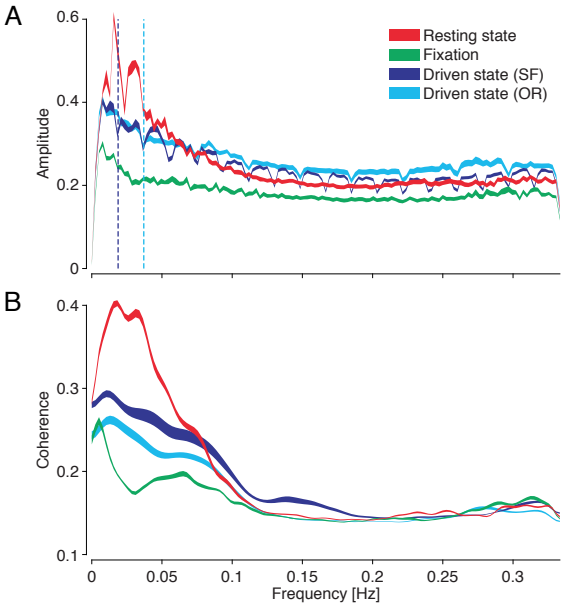

Figure 5. Spectral analysis of moment-to-moment fluctuations in fMRI activity during different viewing conditions

(*A*) Across-voxel and across-subject averages of the amplitude spectra of fMRI activity in V1, V2, and V3 during the different viewing conditions (indicated by different colors). The vertical dashed lines demarcate the temporal frequencies of cycle repetition during the stimulus tuning scans—1/54 Hz for spatial frequency (SF, dark blue line), and 1/27 Hz for orientation (OR, light blue line). Note that the amplitudes of driven-state noises (deviations from the across-cycle average time courses) were suppressed at the harmonic frequencies of stimulus repetition periods because the periodic signals at stimulus frequency have been removed from the original time series. (*B*) Across-voxel-pair and across-subject averages of the coherence in fMRI activity between voxels. The color scheme is identical to that in *A*. Curves and their thickness represent means and s.e.m.s across the seven subjects who participated in the main experiment.

For the voxel pairs in V1, the tuning similarity in SF accounted for the largest fraction of the variance in the resting-state correlation (Fig. 6*A*;

r^2 = 0.312 ± 0.040, mean ± s.e.m. across subjects). The resting-state correlation was lower for voxel pairs with less similar tuning profiles for SF (e.g., green dot in Fig. 3*G*) and substantially increased as the tuning profiles became more similar (e.g., red dot in Fig. 3*G*). The tuning similarity in OR and the two distance factors (RD and CD) also accounted for the variance in resting-state correlation, albeit to a lesser extent than did SF (Fig. 3*H–J*; Fig. 6*A*; r^2 = 0.083 ± 0.016, 0.082 ± 0.013, and 0.071 ± 0.013, for OR tuning similarity, RD, and CD, respectively; see also gray bars in Fig. 6*D*).

However, the tuning similarity factors were substantially correlated with the distance factors in V1 (Fig. 6*B*). The correlations of the SF tuning similarity with the RD and CD were –0.335 (averaged across subjects; s.d., 0.089) and –0.323 (0.073), respectively. Likewise, the correlations of the OR tuning similarity with the RD and CD were –0.309 (0.081) and –0.245, respectively (0.116; *P* values < 0.001 for all of the 28 Pearson's correlation coefficients defined by the seven subjects × four conditions). This interdependence between the tuning similarity factors and the distance factors raises the possibility that the observed contribution of the tuning similarity factors to the resting-state correlation could have simply reflected their relationship with the distance factors. To address this concern, we evaluated the contribution

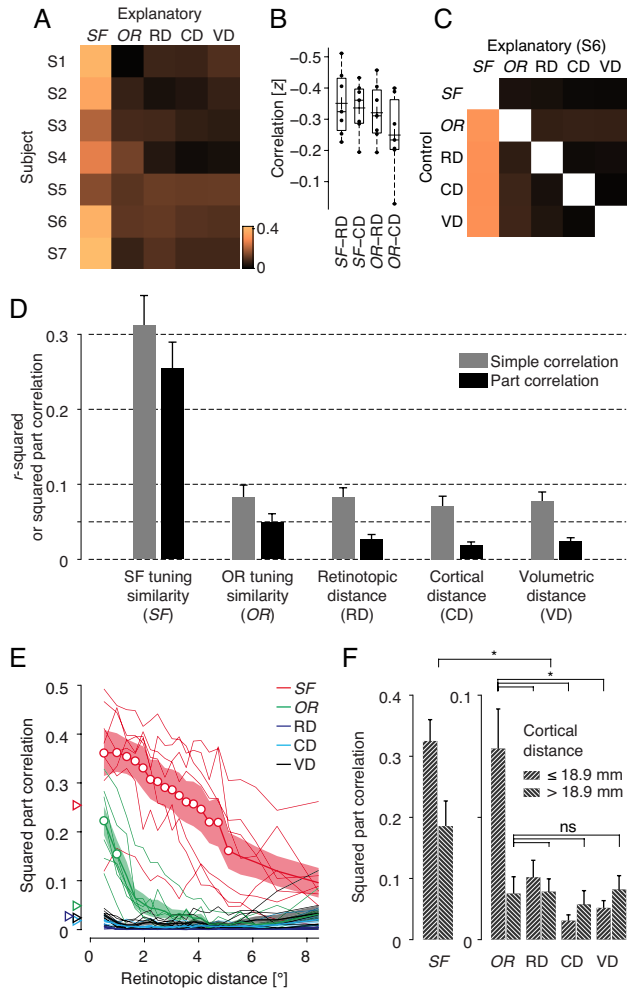

Figure 6. Simple and part correlations of resting-state correlation with three factors in V1

(*A*) A matrix of squared simple correlations of resting-state correlation with tuning similarity and distance factors (columns) for seven subjects (rows). (*B*) Dependency among tuning similarities and RDs and CDs. Dots represent individual subjects, and crosses their averages. (*C*) A matrix of squared part correlations of resting-state correlations with explanatory variables (columns) given the control variables (rows) for a single subject (S6; see MATERIALS AND METHODS for details). (*D*) Population summary of squared simple and part correlations. For each explanatory variable, the squared part correlations were

averaged across the control variables. Bars and error bars, means and s.e.m.s across subjects, respectively. (*E*) Squared part correlations of resting-state correlation with relational factors, plotted against the medians of individual RD bins, which contained the same number of voxel pairs. Thin lines, data from individual subjects. Thick lines with shaded patches, across-subject means with s.e.m.s. Circles indicate the RD bins in which tuning similarity in either SF (red) or OR (green) is significantly larger than all RD, CD, and volumetric distance (VD) in *post hoc* pairwise comparison tests (one-way repeated measures ANOVAs within each RD bin; adjusted *P* values). (*F*) Average squared part correlations of resting-state correlation with relational factors for short (left diagonal hatch) and long (right diagonal hatch) CD regimes, split by the median value of CDs merged across subjects (18.9 mm). Horizontal brackets represent the *post hoc* comparisons for SF and OR vs. RD, CD, and VD (one-way repeated measures ANOVAs; unadjusted *P* values). Error bars, s.e.m.s across subjects.

of each factor to the resting-state correlation while controlling the contributions of the other factors. To remove the joint effects of the explanatory and control variables on the total variance in the resting-state correlation, we used part correlation (see MATERIALS AND METHODS and Fig. 7 for details). To perform exhaustive comparisons, each factor was treated as an explanatory variable (columns in Fig. 6*C*), while the remaining factors were partitioned out one by one as control variables (rows in Fig. 6*C*). To account for the possible contributions of the variance in BOLD fluctuations that were shared among neighboring voxels in the 3D imaging space, we also included the volumetric distance (VD; Euclidean distance in three-dimensional space) in the analysis.

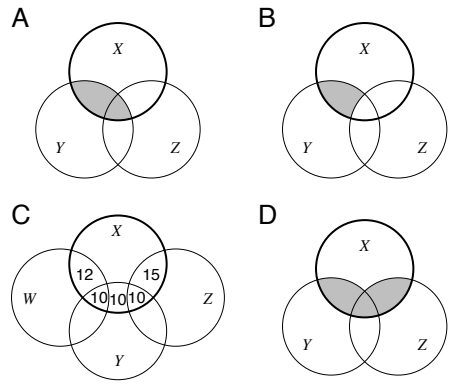

Figure 7. Schematic illustration of simple correlation, part correlation, and multiple regression

Correlation measures the strength of linear association between two variables. When there is only one response variable (X) and one explanatory variable (Y) to consider, the square of a simple correlation coefficient (r_{XY}^2) measures the fraction of variance in X that is explained by Y (A). When there are more than one explanatory variable, the contribution of Y to X can differ depending on what relationship we are interested in and whether explanatory variables are correlated with one another. The square of a part correlation (sr_{XY}^2) quantifies the Y's unique contribution while the contributions from the other explanatory variables were separated out from Y (B). Thus, the part correlation complements the simple correlation in that it isolates the unique contribution of the variable of interest. Note that the squares of the simple and part correlations both share the same denominator, the total variance of the variable X, which is indicated by the thick circle in A and B**.** In some cases, the contributions of explanatory variables can markedly differ between when assessed with simple correlations and when assessed with part correlations. Such a case is illustrated in C. Here, the three explanatory variables (W, Y, and Z) are correlated, and their shared variances are indicated by the percentage numbers in the sub-regions of the diagram. In terms of simple correlation, the contributions of the explanatory variables to the response variable X are in the order of $r_{XY}^2 > r_{XZ}^2 > r_{XW}^2$ (10 + 10 + 10 > 10 + 15 > 10 + 12). In terms of part correlation, they are ordered differently: $sr_{XZ}^2 > sr_{XW}^2 > sr_{XY}^2$ (15 > 12 > 10). Whereas a part correlation is useful in quantifying the "unique" contribution of an explanatory variable to a response variable, we might be also interested in quantifying the collective contribution of more than one explanatory variable to the response variable. This latter quantity can be measured by building a multiple regression model, as indicated by the fraction of the shaded sub-regions to the thick-line circle in D.

Even when the effects of the distance factors were controlled, a substantial fraction of the variance in the resting-state correlation between V1 sites was explained by the tuning similarity factors (black bars in Fig. 6*D*). When the unique contribution to the variance of the resting-state correlation was estimated by squared part correlation, all of the factors that we considered contributed significantly (t_6 = 7.251, P < 0.001, one-sample *t*-test, for SF; t_6 = 4.146, P = 0.006 for OR; t_6 = 4.869, P = 0.003 for RD; t_6 = 3.918, P = 0.008 for CD; t_6 = 5.098, P = 0.002 for VD). However, the contribution differed significantly between the factors ($F_{4,24}$ = 31.954, P < 0.001, one-way repeated measures ANOVA). Specifically, the contribution by the SF tuning similarity factor was the greatest (25.5 ± 3.5 pp [across-subject mean ± s.e.m.] for SF; 2.7 ± 0.6 pp for RD; 1.8 ± 0.5 pp for CD; 2.4 ± 0.5 pp for VD) and significantly surpassed any of the distance factors (P = 0.005 for SF vs. RD, P = 0.004 for SF vs. CD, and P = 0.003 for SF vs. VD, Tukey-Kramer corrected for multiple comparisons). The contribution made by the other tuning similarity factor, OR (4.9 ± 1.2 pp), was also greater than those by any of the distance factors, although the differences were insignificant (P's = 0. 517, 0.283, 0. 522 for OR vs. RD, CD, VD, respectively).

To examine the extent to which the contribution of tuning similarity varies as a function of spatial distance, we divided the same

pools of V1 voxel pairs based on their proximity in retinotopic space. When the squared part correlations were computed over the bins of RD, the contributions of the tuning similarity factors decreased as the RD between the voxels increased (Fig. 6*E*). However, this distance-dependent effect was not observed for the distance factors. Whereas the contribution of the SF tuning similarity outperformed those of the distance factors significantly for the voxel pairs with RD up to 6° (red circles in Fig. 6*E*), the contribution of the OR tuning similarity was significantly greater than those of the distance factors only for the voxel pairs with RD less than 2° (green circles in Fig. 6*E*). A similar trend was observed when the voxel pairs were sorted in terms of CD: the superior contributions of the tuning similarity factors were strong at short CDs (≤ 18.9 mm; one-way repeated measures ANOVA, $F_{4,24}$ = 55.784, P < 0.001; *post hoc* tests showed that largest unadjusted P value was P < 0.001 for SF vs. RD, CD, VD, and P = 0.024 for the comparisons with OR; left diagonal hatched bars in Fig. 6*F*), but became less strong for long CDs (> 18.9 mm; one-way repeated measures ANOVA, $F_{4,24}$ = 13.996, P < 0.001; *post hoc* tests, largest unadjusted P value, P = 0.009 for SF vs. RD, CD, VD, and the comparisons with OR were all insignificant; right diagonal hatched bars in Fig. 6*F*).

Having observed the predominant contribution of tuning similarity, in SF particularly, to the structure of resting-state correlations within V1, we performed the same analyses for V2 and V3 (hereafter referred to as V2/V3). To ensure unbiased comparisons across the areas, the voxel pair pools for V1 were redefined to match those for V2/V3 by splitting up the dorsal and ventral subregions around the horizontal meridian (areas between dashed lines in the right panel in Fig. 2*B*). These within-quadrant pools were necessary for avoiding the unwanted disadvantages for the areas V2/V3 in terms of CDs. We note that this restriction becomes unnecessary if only the RD is considered as a distance factor, and the results on the pools unrestricted to the visual quadrants will be addressed later when comparing the tuning similarity and the RD factor (see ***Invariance of Stimulus-Tuned Covariability to Changes in Spatial Scale***).

As observed in V1, the tuning similarity made the largest contribution to the resting-state correlations in V2/V3, but with OR, not SF (Fig. 8*A*). When the variances explained by the tuning similarity factors were plotted against the distance factors, the predominance of SF and OR tuning similarities decreased gradually over CD (Fig. 9). But unlike in V1, the contribution of OR similarity factor to resting-state correlation remained significant over those of distance factors even for

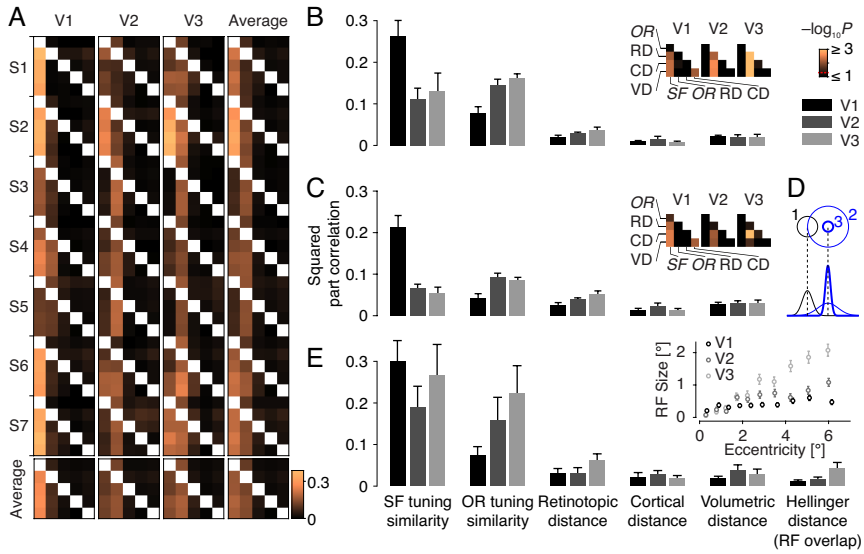

Figure 8. Contributions of three relational factors to resting-state correlations in V1, V2, and V3

(*A*) Matrices of squared part correlations of resting-state correlations for individual subjects and visual areas. The format of the matrix for an individual subject and area is identical to that in Fig. 6*C*. (*B*) Population summary of the data shown in *A*. (*C*) Population summary when the tuning similarities were defined from non-concurrent time series (see text). (*B*,*C*) The matrices in the inset shows the significance values of the pairwise comparisons (Sidak's corrected). Red dotted line in the color bar indicates $P = 0.05$. Bars and error bars, means and s.e.m.s, respectively, across subjects from the main experiment (N = 7). (*D*) Illustration of a discrepancy between RD and RF overlap. The center-to-center distance is identical between the site 1 (black)-2 (thin blue) pair and the site 1-3 (thick blue) pair, whereas the fraction of shared retinal input is greater in the site 1-2 pair than in the site 1-3 pair. (*E*) Population summary of the data from the auxiliary experiment, in which RF overlap for voxel pairs was estimated (see MATERIALS AND METHODS). The format is identical to that in *B*. Bars and error bars, means and s.e.m.s across subjects (N = 5). In the inset, RF sizes as measured by the sigma values of the estimated pRFs are plotted against eccentricity, separately for V1, V2, and V3.

the voxel pairs more than 10 mm apart in V2/V3 (the middle and right panels in Fig. 9*B,C*). The contributions of two distance factors, RD and CD, were negligible, and thus the distance-dependent effects were not evident for the RD and CD factors in any of the visual areas. In contrast, we note that the contribution of the VD factor to resting-state correlation tended to increase sharply for the voxel pairs with CDs of less than 10 mm in all of the three visual areas (black curves in Fig. 9*B,C*). These high correlations between neighboring voxels may reflect the intrinsic spread of the BOLD signal (Engel et al. 1997).

To test whether the mean contribution to the resting-state correlation significantly differed over the relational measure types (SF and OR tuning similarities, RD, CD, and VD) and the visual areas (V1, V2, and V3), we performed a two-way (five measure types × three areas) repeated measures (subject as blocking variable, N = 7) ANOVA. The relational measure types significantly interacted with the visual areas ($F_{8,48}$ = 16.730, P < 0.001). In V1, the tuning similarity in SF made the largest contribution to the resting-state correlation (sr^2 = 0.263 ± 0.037, mean ± s.e.m. of squared part correlations across subjects), and its contribution was significantly greater than those by the distance factors (P's = 0.008, 0.005, 0.005 for SF vs. RD, CD, VD on sr^2, respectively, adjusted using the Sidak method; Fig. 8*B*). In V2 and V3, by contrast, the

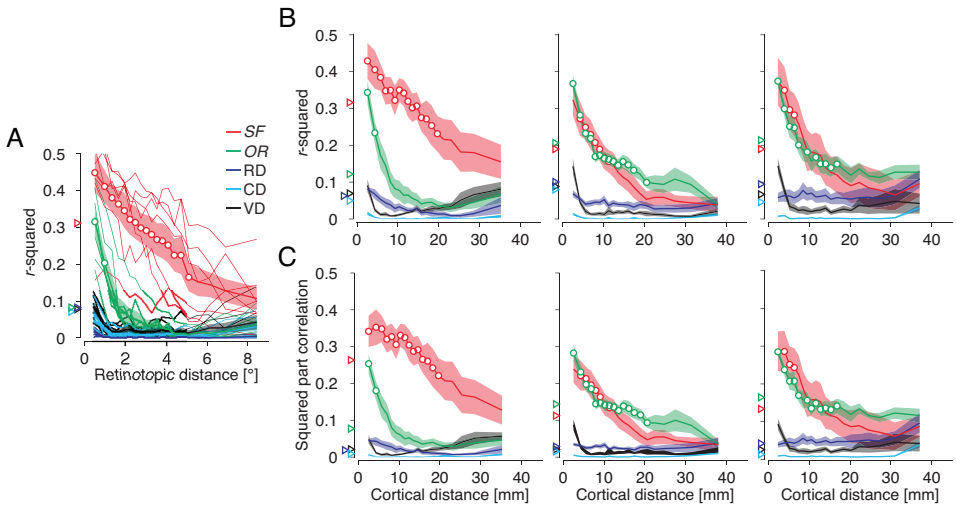

Figure 9. Contributions of tuning similarity and distance factors as functions of retinotopic and cortical distances in V1, V2, and V3

To examine how the five relational factors' power of explaining the variations in the resting-state correlations varied across the different regimes of the distances between voxels, we plotted the explained variances against RDs (*A*) and CDs (*B*,*C*). The *x*-coordinates are the median distance values of the discrete bins containing 5 % of total number of voxel pairs, as similarly done in Fig. 6*E*. The variances explained by each factor was measured by either simple correlations (*A*,*B*) or by part correlations (*C*). The circles demarcate the bins in which the variance explained by tuning similarity in SF (red) or OR (green) was significantly greater than all of the RD, CD, and VD (*post hoc* pairwise comparison tests after one-way repeated measures ANOVAs; *P*'s adjusted). The explained variances for the entire set of voxels pairs (without binning) are displayed as the colored triangles on the *y*-axis in each panel (only across-subject means displayed here for simplicity). (*A*) The results for the "within-V1" condition, same as in Fig. 6*E*, except for that explained variances were measured by simple correlations. A cautionary interpretation of the plots is required here: any non-zero individual *r*-squared values in these plots only indicate the existence of some explanatory power in a given specific distance regime. For this reason, note that, even when constant zeroes of *r*-squared values (or squared part correlations as shown in Fig. 6*E*) are observed across all distance regimes (bins), it does not necessarily mean that there is no contribution. This is why the explained variances without binning (the colored triangles on the *y*-axes) were similar between OR and RD, but substantially differed when measured as function of distances (curves). The local contributions for all factors—including RDs and CDs—were pronounced at short (less than 2°) range of RD, which was not readily recognizable in Fig. 6*E* for part correlation analyses. Nonetheless, the contributions of the tuning similarity factors outperformed those of the distance

factors for those short ranges. (*B*) and (*C*) The contributions of the tuning similarity and distance factors in V1, V2, and V3 (left, middle and right panels, respectively) as a function of CD. For V1 (left panels), unlike in *A*, we analyzed the data within the same dorsal/ventral sub-regions separately, as similarly done in Fig. 5. Without such dorsal/ventral division, the CD factors will have unfair disadvantage in explanatory power compared to when inspected within V1, because V2 and V3 areas are geometrically separated while V1 is not (for the results without dorsal/ventral division without CD and VD factors, see Figs. 19 and 20). The contribution of the OR tuning similarity at the long distances was more pronounced in V2/V3 than in V1, whereas the SF tuning similarity's contribution was reduced overall throughout the entire CD regimes. As expected, the explained variances appeared to be reduced when expressed in squared part correlation coefficients (*C*), compared to when expressed in simple correlation coefficients (*B*). (*A*–*C*) All data from the same hemispheres (for results without hemispheric division in V1, see Fig. 19*A*). Thin lines in *A*, data from individual subjects. Thick lines with shaded patches, across-subject means with s.e.m.s from the main experiment (N = 7).

tuning similarity in OR showed the largest contribution (sr^2 = 0.144 ± 0.015 and 0.162 ± 0.010 for V2 and V3, respectively), and the contribution of the OR similarity was significantly greater than those made by the distance factors (largest *P* value, *P* = 0.007 for OR vs. RD, CD, VD in V2; all *P*'s < 0.001 for the same comparisons in V3; adjusted *P* values; Fig. 8*B*). In addition, we confirmed that these results were not the consequence of biased sampling introduced by the particular set of voxel selection criteria adopted in this study (Fig. 10; see subsection ***Voxel Selection*** in MATERIALS AND METHODS).

Thus, we conclude that the similarity in stimulus tuning is the strongest factor explaining the variance in resting-state correlation in the early visual cortex. The contribution of tuning similarity was greatest at

short RDs and CDs. The tuning similarity factors, although the amount of their contributions varied over the visual areas and the stimulus types with which tuning similarity was estimated, were invariably superlative in explaining the variance in correlated resting-state activity to any of the distance factors, including the distances defined over the visual field, cortical surface, or brain volume.

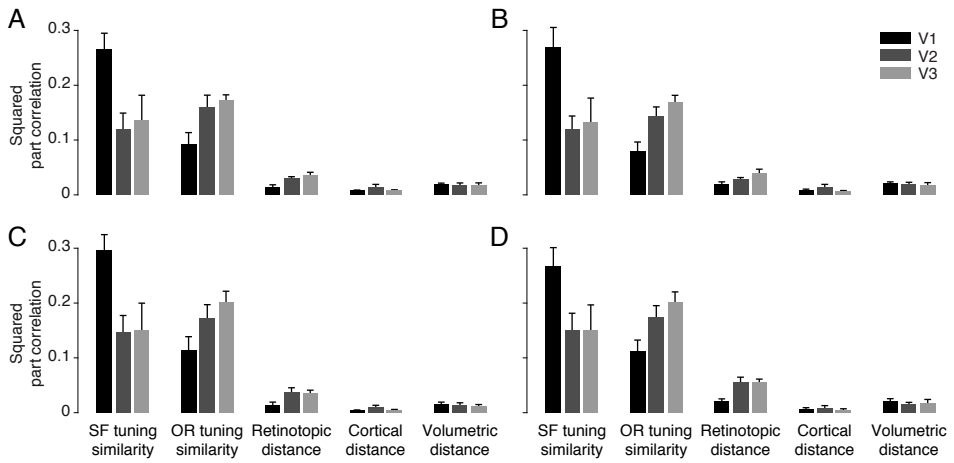

Figure 10. Predominance of tuning similarity invariant to various voxel selection criteria

To examine the impacts of voxel selection criteria on the predominance of tuning similarity factors over the distance factors in governing the structure of resting-state correlation, we created the four different sets of voxel selection criteria and inspected how the squared part correlation coefficients varies across those different sets. (*A*) The results when we selected the voxels whose s.d.s were less than the 10th percentile rather than the 20th percentile (graphically put, the vertical dashed lines were shifted to the right in Fig. 4*B*). (*B*) The results when we selected the voxels whose SNRs were higher than 1.5 rather than 2.0 during the on-/off-stimulation scans (graphically put, the vertical dashed lines were

shifted to the left in Fig. 4*C*). In both *A* and *B*, we kept all the other remaining criteria the same as those in the original set shown in Fig. 4. (*C*) The results when we did not apply any of the criteria based on the s.d.s (Fig. 4*B*), SNRs (Fig. 4*C*), or temporal phase values (Fig. 4*D*) but only applied the criterion based on the deviations from neighboring voxels' RF positions (Fig. 4*G*). (*D*) The results when we used the entire set of voxels without applying any of the four criteria. The two-way repeated measures ANOVAs showed the significant interactions between the relational measure types and the visual areas on the effects of the squared part correlations in all conditions (smallest $F_{8,48}$ = 10.673, and the corresponding P < 0.001, across four conditions in *A*–*D*). In all conditions, the contribution of SF tuning similarity was greater than those of the distance factors in V1 (SF vs. RD, CD, or VD, the maximum adjusted P = 0.007), and the contribution of the OR similarity factor was greater than those of the distance factors in V2/V3 (OR vs. RD, CD, or VD, the maximum adjusted P = 0.048). The average number of the valid voxels used for the newly created set of voxel selection criteria were as follows: 1356.1 (47.5 % of the total, 285.3) ± 94.4 (s.e.m.) for *A*, 1314.6 (46.1 %) ± 86.1 for *B*, and 1780.4 (62.4 %) ± 106.1 for for *C*, Bars and error bars, across-subject means and s.e.m.s from the main experiment (N = 7).

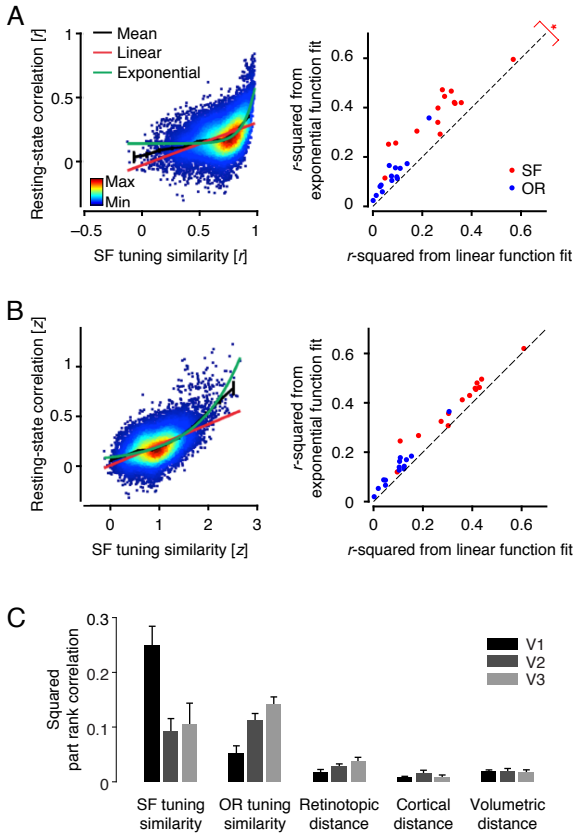

Figure 11. Improved linearity of relationship between the *z*-transformed values of resting-state correlation and tuning similarity factors and results of part rank correlation analyses

Linear regression assumes that two variables are related in a close-to-linear manner. We checked the linearity of our data by comparing the *r*-squared values from linear and non-linear function fits respectively, before and after the Fisher's *z* transform (*A*,*B*). To further address any non-linear relationship between variables, we also performed rank correlation and part rank correlation analyses (*C*). (*A*) The relationship between resting-state correlation and tuning similarity was non-linear, when their original values (in Pearson's *r* unit) were pitted against each other. The left panel shows the joint histogram of resting-state correlation and SF tuning similarity from the left hemisphere of a representative subject's V1. The color of a dot (a voxel pair) represents a joint probability (200 by 200 bins, smoothed). The exponential function (green curve) was fit better to the data than the linear function (red line) was. The right panel shows the

population results, where the individual data points represent 14 V1 areas from the both hemispheres of 7 subjects. A greater fraction of variance was explained by the exponential fit than by the linear fit (two-sample *t*-test on *r*-squared values from exponential fit vs. *r*-squared values from linear fit, $P = 0.032$ for SF, and $P = 0.089$ for OR). (*B*) Left, the same data in the left panel of *A* are shown, except for that both the resting-state correlations and the tuning similarities were transformed by Fisher's *z*. Right, the differences in explained variance between the exponential and linear fits were substantially reduced after the transformation (two-sample *t*-test on *r*-squared values from exponential fit vs. linear fit, $P = 0.334$ for SF, and $P = 0.251$ for OR). This indicates that the relationship between resting-state correlation and tuning similarity became more linear after *r*-to-*z* transformation, thus we decided to use the *z*-transformed data for the simple correlation, part correlation and multiple regression analyses. In an additional analysis, the retinotopic distances (RDs) and cortical distances (CDs) were transformed into $\log_{10}$ values, but the results were largely unchanged (data not shown). (*C*) The part rank correlations of the resting-state correlation with the tuning similarity and distance factors. The format is identical to that of Fig. 8*B*, except for that the part correlations were computed from the ranks of the original *r* and distance values. The two-way repeated measures ANOVA showed the significant interactions between the relational factors and the visual areas on the effect of the squared part rank correlations ($F_{8,48} = 16.069$, $P < 0.001$). The *post hoc* analyses showed that the contribution of the SF tuning similarity to the resting state correlations in V1 was significantly greater than that of the distance factors (largest adjusted $P = 0.007$ for SF vs. RD, CD, and volumetric distance [VD]), whereas that of the OR tuning similarity in V2 and V3 was significantly greater than that of the distance factors (largest adjusted *P*'s = 0.014 and 0.003 in V2 and V3 respectively, for OR vs. RD, CD, VD). These results are consistent with those described in Fig. 8*B*. Bars and error bars, across-subject means and s.e.m.s from the main experiment (N = 7).

2.3. Controls for Alternative Explanations

In our results, the contribution of RD and CD factors to the variability in resting-state correlation was moderate when assessed by simple correlation, and even further reduced when their correlations with the other factors were controlled for. This may appear as a somewhat unexpected outcome given the previous fMRI studies that reported the dependence of resting-state correlation on RD or CD (Heinzle et al. 2011; Butt et al. 2013; Gravel et al. 2014; Raemaekers et al. 2014; Arcaro et al. 2015). Thus, we wondered whether there is any possibility that the contribution of distance factors to correlated activity was underestimated, or, similarly, that the contribution of tuning similarity was overestimated due to any aspects of the methods or procedures adopted in this study. To address these concerns, we generated a set of alternative hypotheses for the observed superiority of tuning similarity and ruled them out individually by carrying out control analyses or collecting additional data under different conditions.

Shared ongoing activity. Ongoing BOLD activity exhibits widespread correlation patterns throughout the cortex (Schölvinck et al. 2010), implying that the profiles of responses to the stimuli used for defining tuning similarity (e.g., shown in Fig. 3*C,D*) could have included not only a stimulus-driven component but also a stimulus-independent, ongoing activity component, particularly in the voxels with low SNRs. This could have resulted in response profiles that have been synchronized to some degree for voxel pairs, irrespective of their stimulus tuning similarity. Thus, there is a possibility that the observed high correlation between stimulus tuning similarity and resting-state correlation could have arisen partly from the correlated ongoing activities, if we assume that ongoing and resting-state activities are generated via similar neurophysiological mechanisms. To address this concern, we redefined the tuning similarity based on the fMRI time series that were acquired during non-overlapping periods of time. The fMRI time courses of all voxels during the stimulus tuning scans were randomly split into two disjoint sets of cycles. Next, for any given voxel pairs, the responses of one voxel were averaged across the cycles belonging to the first set, and the responses of the other voxel were averaged across the second set of cycles. This procedure was repeated many (20) times, resulting in multiple correlation measures for SF and OR, respectively, for each voxel pair. The tuning similarity was

defined as the average of those multiple correlation values. Then, the part correlation analysis was carried out using these alternative tuning similarity measures. Even when comparing the squared part correlations computed from these "ongoing activity-free" measures of stimulus tuning similarity (interaction effect found, $F_{8,48} = 25.948$, $P < 0.001$, from two-way repeated measures ANOVA), we found that the contribution of SF was strong in V1 (Fig. 8*C*; largest $P = 0.006$ for SF vs. RD, CD, VD in *post hoc* tests; *P*'s adjusted) whereas the contribution of OR was strong in V2/V3 (Fig. 8*C*; $P = 0.055$ for OR vs. RD, and *P*'s = 0.008 and 0.009 for OR vs. CD and VD respectively in V2; largest $P = 0.046$ for OR vs. RD, CD, VD in V3).

Receptive field overlap. We considered the possibility that the degree of RF overlap (Fig. 8*D*), as an alternative metric for the RD factor, could better explain the variance in correlated spontaneous activity than the tuning similarity could. To check this possibility, we carried out an auxiliary experiment in which both the RF proximity and the similarity in RF shape were characterized by BOLD response profiles to a thin bar drifting in eight successively different directions over the visual field (see MATERIALS AND METHODS for details).

The population receptive fields (pRFs) of individual voxels were estimated using the isotropic bivariate normal distributions to the response profiles (Fig. 8*E*, inset), and the RF overlap was defined by the Hellinger distance (HD) between two pRFs, measuring how much those distributions were matched ($d_{\text{Hellinger}}$; Fig. 18*A*; see MATERIALS AND METHODS). We also computed the correlation between BOLD response profiles to moving bars themselves for any given voxel pair and used it as a non-parametric proxy for RF overlap. These correlation-based estimates have an important advantage over the HD estimates: they allow for the retinotopic proximity being defined in the same manner as the tuning similarity, and the resting-state correlation as well, so that any unknown confounding factors due to the different ways of estimating the relational factors can be precluded.

Despite a smaller number of subjects in the auxiliary experiment (N = 5), the overall pattern of results was similar to that from the main experiment. The relational measure types and the visual areas significantly interacted with one another in explaining the variance in correlated resting-state activity (two-way repeated measures ANOVA, $F_{10,40}$ = 2.165 and P = 0.041 for six measure types × three visual areas), and the following *post hoc* pairwise comparisons showed that SF tuning similarity factor outperformed distance and RF overlap factors in V1 and

V2 (largest unadjusted *P* values: *P*'s = 0.007 and 0.037 in V1 and V2, respectively; Fig. 8*E*), whereas, in V3, the superiority of OR tuning similarity was marginally significant (unadjusted *P* values: *P*'s = 0.050, 0.040, 0.058 for OR vs. CD, HD, VD, respectively; Fig. 8*E*) except for the comparison with RD (unadjusted *P* = 0.105; Fig. 8*E*). Additionally, the

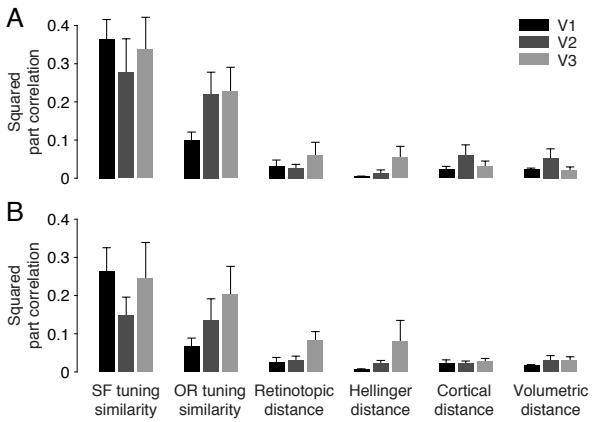

Figure 12. Effects of receptive field overlap on the stimulus-tuned covariability of resting-sate activity

We showed that the contribution of RF overlap factor, as measured by the squared part correlation with HD, was smaller than those of tuning similarity factors (Figs. 8*C,D* and 18). To provide converging evidence for this, the squared part correlations were also computed for the voxel pairs whose HDs were shorter (more RF overlap; *A*), or longer (less RF overlap; *B*) than the median HD of the voxel pairs with RDs less than 2°. The results were in agreement with those shown in Fig. 8*D*: the contributions of the tuning similarity factors were greater than those of all the distance factors including RD, CD, VD and HD for both of the voxel-pair groups with high and low degrees of RF overlap. Bars and error bars, across-subject means and s.e.m.s from the auxiliary experiment (N = 5).

superiority of tuning similarity factors held not only for the voxel pairs with low degrees of RF overlap, but also for those with high degrees of RF overlap (Fig. 12). Lastly, we also confirmed that the direct correlation measures of RF overlap did not surpass the power of the tuning similarity factors in explaining the variance of resting-state correlation (Fig. 13).

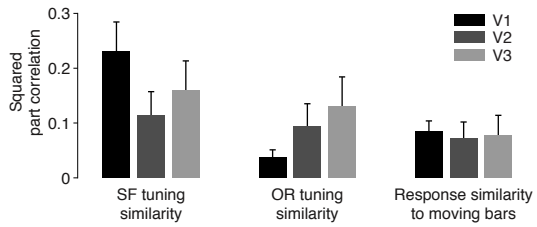

Figure 13. Results from alternative distance measures, correlations in time series of fMRI responses to moving bar stimuli

Although the time series of fMRI responses to moving bars were analyzed for the purpose of estimating the population receptive fields (pRFs) of individual voxels, their correlations between voxels could also be used to quantify the spatial distance in the same way the tuning similarity and resting-state correlation were measured. For each voxel pair, the correlations between their across-cycle averages of fMRI responses to the moving bar stimuli were computed separately for the eight moving directions and then averaged. Bars and error bars, across-subject means and s.e.m.s from the auxiliary experiment (N = 5).

Coincidence between eccentricity and SF preference or between angular position and OR preference. We demonstrated the strong contributions of SF and OR tuning similarities to the resting-state correlations. However, those similarity measures were highly correlated with eccentricity and angular position differences in retinotopic space (Fig. 2*G*). Thus, we

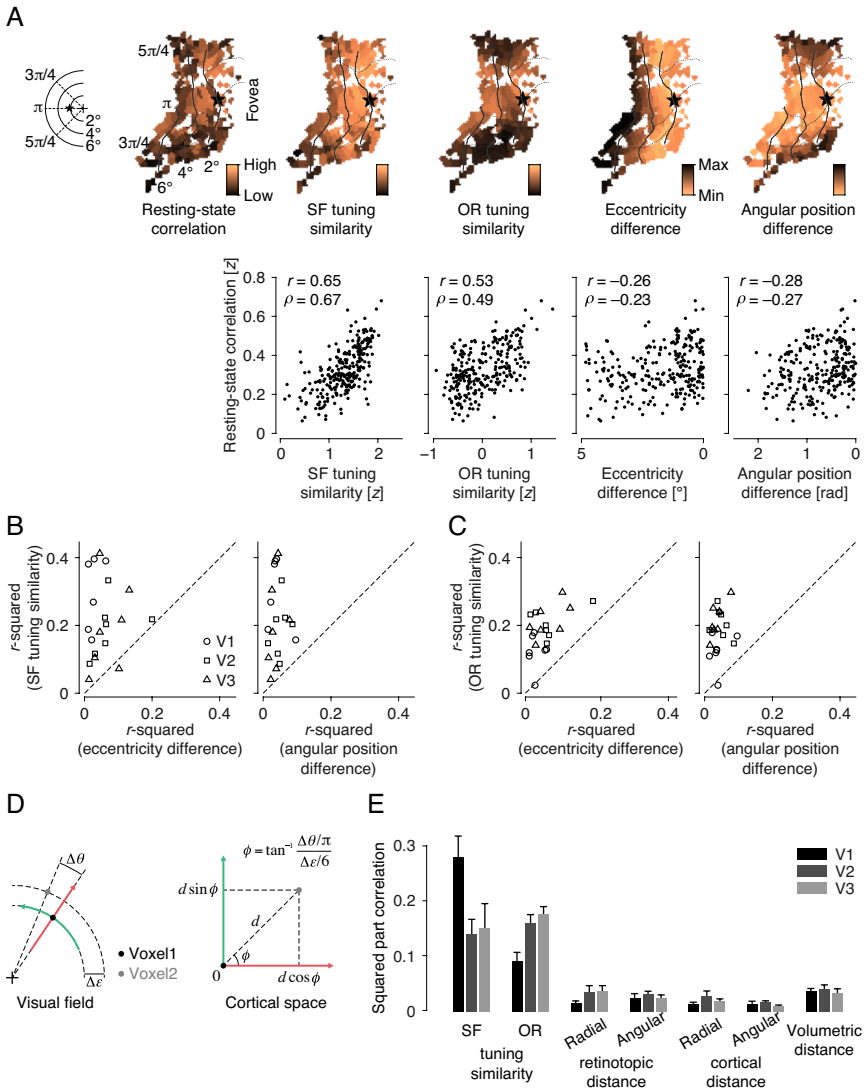

considered the possibility that the distances defined along axes of the polar-coordinate system could better explain the variance in resting-state correlation, as reported by a recent study (Arcaro et al. 2015), and surpass the explanatory power of tuning similarity. To check this possibility, we decomposed the RD for any given voxel pair into the distance along the radial axis (iso-angular lines) and the distance along

Figure 14. Results based on spatial distance measures defined along polar-coordinate axes

(*A*) Relationship of tuning similarity and radial or angular distance in the visual field with resting-state correlation. Top row, relationships of a seed voxel (marked as a star) with the rest of voxels projected onto the flattened surface of a representative subject's right-hemisphere V1. Solid and dotted curves on the cortical surface delineate the iso-eccentricity half circles and iso-angle meridians, respectively, drawn on the visual field in the leftmost panel. Bottom row, scatter plots showing the relationship between the resting-state correlation (the leftmost panel in the top row) and the tuning similarity (second and third panels from the left in the top row) or alternative retinotopic (the two rightmost panels in the top row) factors. (*B,C*) Population summary of the variances in resting-state correlations explained by the tuning similarity factors (SF in *B*, OR in *C*) pitted against those explained by the eccentricity (left panels) and angular position difference (right panels) factors. Data points represent individual subjects for visual areas, which are indicated by different symbols. (*D*) Definition of angular and radial distances in visual field (left), and in cortical surface (right). The red and green lines with arrowheads are the radial and angular axes of a reference voxel (black dot), respectively, defined in the visual field. In the cortical surface, radial and angular distances were estimated by multiplying the CD (demarcated as d) with the cosine and sine, respectively, of the angle (ϕ) formed by vector ($\Delta\epsilon$, $\Delta\theta$), where the horizontal and vertical axes are defined as eccentricity ($\Delta\epsilon$) and angular position differences ($\Delta\theta$), respectively. Here $\Delta\epsilon$ and $\Delta\theta$ were normalized between 0 and 1 within each dimension before taking their arc tangent values. (*E*) Population summary of squared part correlations when angular and radial distances are considered as alternative measures for distance factors. Bars and error bars, across-subject means and s.e.m.s (N = 7).

the angular axis (iso-eccentricity lines) in retinotopic space ($d^R_{\text{retinotopic}}$ and $d^A_{\text{retinotopic}}$, respectively; Fig. 14*A*). Likewise, we also decomposed the CD between cortical sites into one along the radial axis and the other along the angular axis by projecting the CDs onto radial and angular axes in visual space (d^R_{cortical} and d^A_{cortical}, respectively; Fig. 14*D*). The simple correlation analysis showed that the variances in correlated activity explained by the SF and OR tuning similarities were much higher than those by the radial or angular distances in retinotopic space (Fig. 14*A*–*C*). The tuning similarity factor remained substantial in both retinotopic and cortical spaces even when the effects of these alternative distance measures' contributions were controlled (two-way repeated measures ANOVA with seven relational measure types and three visual areas used as within-subject factors; significant interaction, $F_{12,72} = 13.983$, $P < 0.001$; *post hoc* tests showed SF tuning similarity outperformed all distance factors in V1, with largest adjusted $P = 0.018$, whereas OR tuning similarity outperformed, with largest adjusted values for *P*'s = 0.010 and 0.001 in V2 and V3, respectively; Fig. 14*E*).

Reliability of retinotopic mapping estimation. Next, we examined the possibility that the inferior contribution (relative to those for the tuning

similarity factors) of the RD factor to correlated activity might be related to the reliability of our RD measurements. To check this possibility, we divided individual voxels into two groups based on how similar their BOLD response profiles to the retinotopic mapping stimuli were throughout fMRI scans. The contribution of RD was slightly higher in the high reliability group than in the low reliability group. However, the contributions of the tuning similarity factors were also higher to similar degrees in the high reliability group than in the low reliability group. As a result, the RD factors remained substantially inferior to the tuning similarity factors in both the low reliability and high reliability groups (see Fig. 15 for procedures and results), suggesting that the superiority of tuning similarity is unlikely to be ascribed to the unreliability of retinotopic mapping estimation in our experiments.

In sum, our original findings described in the previous section survived all the concerns we considered based on previous studies. Thus, we conclude that the superiority of tuning similarity as a factor determining the structure of the resting-state covariability found in this study is unlikely to be ascribed to any suboptimal or unfair definitions of the distance or tuning similarity measures.

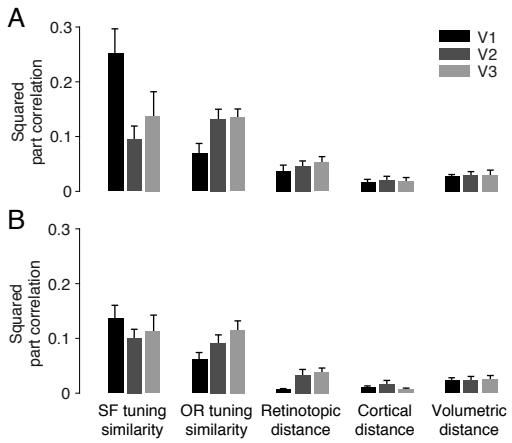

Figure 15. Effects of the reliability in retinotopic mapping on the predominance of tuning similarity factors over distance factors

We wanted to know whether the SNRs of voxels during the retinotopic mapping scans affected the explanatory power of the RD factors, relative to that of the tuning similarity factors. To do so, we first divided the original datasets into even- and odd-numbered scans. Then voxels were categorized into two groups, (*A*) the "high repeatability group" with the correlations between the fMRI responses from even- and odd-numbered scans above 0.9 for all wedge and ring scans (mean [s.d.] across subjects, r = 0.973 [0.004]; number of voxels mean ± s.e.m. across subjects, 817.1 ± 109.9), and (*B*) the " low repeatability group" otherwise (r = 0.896 [0.011]; 683.9 ± 46.1 voxels per subject). For both groups of voxel pairs, we found significant interaction effects ($F_{8,48}$ = 2.804 and P = 0.012 for low repeatability group, and $F_{8,48}$ = 9.232 and P < 0.001 for high repeatability group; two-way repeated measures ANOVA). The squared part correlations for the RD factors were quite similar between the two groups, being only slightly higher in the high repeatability group than in the low repeatability group. According to the simple main effect analyses, the squared part correlations for the tuning similarity factors were generally higher than the RD factors both in the high repeatability group (SF vs. RD in V1, P = 0.069; OR vs. RD in V2 and V3, P = 0.010 and 0.019 respectively; P's adjusted) and in the low repeatability group (SF vs. RD in V1, P = 0.015; OR vs. RD in V2 and V3, P = 0.287 and 0.017 respectively; P's adjusted), indicating the robust predominance of the tuning similarity factors over other distance factors, including the RD factors. Bars and error bars, across-subject means and s.e.m.s from the main experiment (N = 7).

In the remaining sections, we further characterized the predominance of tuning similarity in spontaneous correlated activity in the following three aspects. First, we quantified the fraction of the total variance in the resting-state correlation that could be explained by the two tuning similarity factors, SF and OR, together. Second, we examined whether the presence of external stimulation affected the structure of correlated activity. Finally, we tested whether the stimulus-tuned structure of correlation holds true even between the voxels that are apart at larger spatial scale, beyond the same visual quadrant.

2.4. Combined Contribution of SF and OR Tuning Similarities to Resting-State Correlation

In the previous analyses, we assessed the contribution of each factor separate from the resting-state correlation by computing simple (Fig. 7*A*) and part correlations (Fig. 7*B*), the latter of which allowed us to separate the variance that could be jointly explained with the remaining factors. Here, we quantified the combined contribution of the two tuning similarity factors (Fig. 7*D*) by regressing the resting-state correlation (z_{rest}) on the tuning similarities in SF and OR (z_{tuning}^{SF} and z_{tuning}^{OR}, respectively) together using the following multiple regression model:

$$z_{\text{rest}} = \beta_0 + \beta_1 z_{\text{tuning}}^{SF} + \beta_2 z_{\text{tuning}}^{OR} + \varepsilon.$$

For comparisons, multiple regressions were also performed for the RD and CD factors using the following models:

$$z_{\text{rest}} = \beta_0 + \beta_1 d_{\text{retinotopic}}^{A} + \beta_2 d_{\text{retinotopic}}^{R} + \varepsilon;$$

$$z_{\text{rest}} = \beta_0 + \beta_1 d_{\text{cortical}}^{A} + \beta_2 d_{\text{cortical}}^{R} + \varepsilon.$$

For the resting-state correlations between voxels within V1 (magenta circles in Fig. 16*A*), the regressors of tuning similarity accounted for 37.3 ± 2.9 pp (across-subject mean ± s.e.m.) of the total variance, which was substantially higher than the amounts of variance explained by the retinotopic (7.0 ± 1.3 pp) or cortical (5.2 ± 1.1 pp) distance regressors. The tuning similarity regression was also superior to the other regressions for V2 (magenta squares in Fig. 16*A*; 31.4 ± 2.0 pp) and V3 (magenta triangles in Fig. 16*A*; 33.3 ± 4.7 pp). In addition, to examine the structure of resting-state correlations between visual areas, we selected voxel pairs representing the same visual quadrant as described earlier (see the fourth-to-last paragraph under the heading ***Stimulus-Tuned Covariability in V1, V2, and V3 during the Resting State***). The tuning similarity regressors remained superior to the distance regressors for the between-area voxel pairs (green symbols in Fig. 16*A*; percentages of explained variances averaged across subjects were 18.3 ± 1.0 pp, 24.0 ± 3.2 pp, and 14.9 ± 1.0 pp for V1-V2, V2-V3, and V1-V3 pairs, respectively), although the explained variances were significantly reduced compared with those for the within-area pairs ($P < 0.001$, paired-sample *t*-test; comparison between the green and magenta symbols for the resting-state condition in Fig. 16*B*).

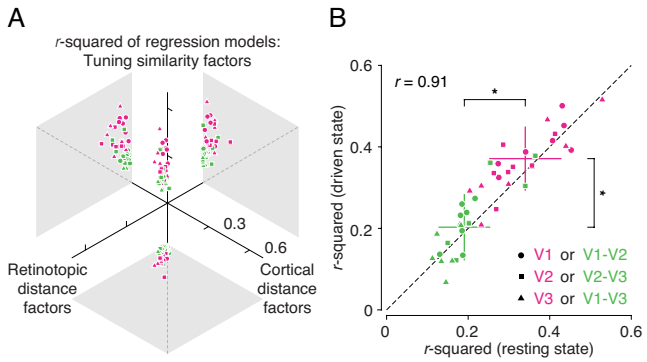

Figure 16. Stimulus-tuned covariability invariant to sensory drive changes

(*A*) Explained variances of three multiple regression models during the resting state. Symbols (42 total) correspond to all combinations of six visual area conditions (three within-area + three between-area) and seven subjects. For comparison between two regression models, symbols are also projected onto two-dimensional planes (gray rhombi) between axes. (*B*) Comparisons of the fractions of variance explained by tuning similarity factors between the eyes-closed (resting state) and the fixation with high contrast (driven state) conditions. The crosses represent the means and standard deviations of the within-area (magenta) and between-area (green) voxel pairs.

2.5. Invariance of Stimulus-Tuned Covariability to Changes in Sensory Drive

To determine whether an increase in sensory drive affects the relative contributions of the three relational factors to correlated activity, we collected BOLD time-series data under two additional conditions. Here, subjects opened their eyes and fixated on small dots at the center of the screen, which was maintained at a fixed luminance (fixation with zero contrast) or displayed a dynamic high contrast stimulus (fixation with high contrast). The raw data for the latter condition were acquired during the scans from which we estimated the tuning profiles for SF and OR. Unlike the original resting-state and fixation with zero contrast conditions, in which the correlations between the raw data were analyzed, for the condition of fixation with high contrast, we analyzed the correlations between the time-series data that deviated from the mean responses to the repeated stimulus cycles (see MATERIALS AND METHODS for details). These correlations will be referred to as driven-state correlations, in contrast to resting-state correlations.

Despite salient changes from the original resting-state condition, the tuning similarity factors remained superior in explaining the variance in correlated activity under both conditions of fixation with zero contrast and fixation with high contrast, when examined for simple correlations (data not shown), for part correlations (Fig. 17*A* and *C* for the zero and high contrast conditions, respectively), and for multiple regressions (Fig. 17*B* and *D* for the zero and high contrast conditions, respectively). In addition, similar to the resting-state condition, the superiority of tuning similarity regressors held true both within and between the visual areas

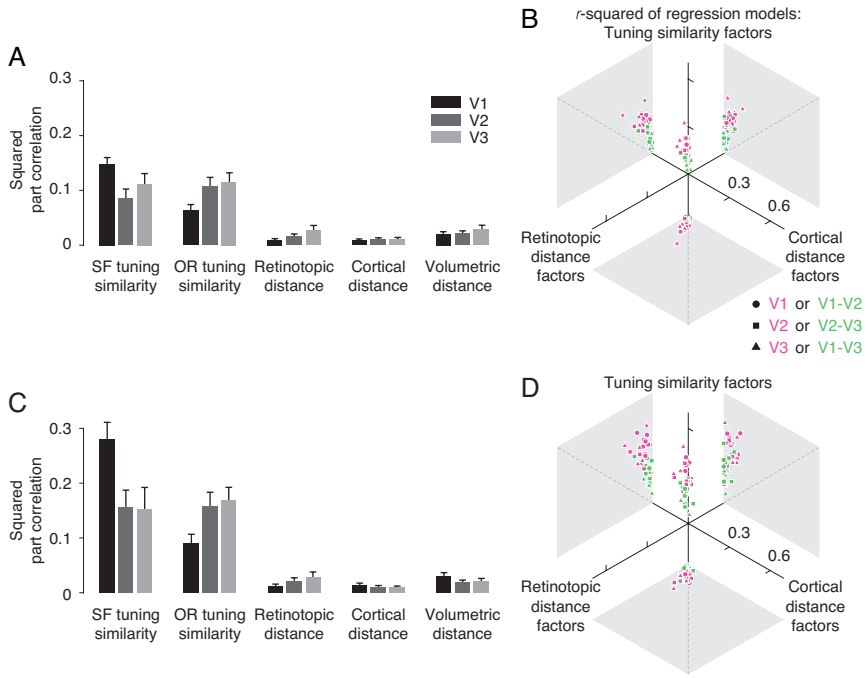

Figure 17. Replication of stimulus-tuned covariability in the "fixation with zero contrast" and "fixation with high contrast" conditions

(magenta and green symbols, respectively, in Fig. 17*B* and *D*).

The invariance of stimulus-tuned covariability to changes in sensory drive was evident, as indicated by the fact that the 42 *r*-squared values of the regressors for tuning similarity factors, obtained from combinations of the six within-/between-area pairs and seven subjects, were highly consistent between the resting-state and the driven-state conditions. As in the resting state, the explained variances were

The scanning procedure was identical to that used for acquiring the resting-state correlation data except for that subjects fixated on the center of the screen while viewing the uniform gray background. (*A*) Squared part correlations of the correlation in the "fixation with zero contrast" condition with the five relational factors. The contributions of the SF and OR tuning similarity factors were greater than those of the distance factors (two-way repeated measures ANOVA, $F_{8,48}$ = 7.107, $P < 0.001$ for measures × areas; largest $P = 0.001$ for SF vs. RD, CD, VD in V1, whereas largest *P*'s = 0.017 and 0.012 in V2 and V3 for comparisons with OR; *P*'s adjusted), although the absolute amounts of contribution decreased in overall, compared to the resting-state (eye closed) condition. Bars and error bars, across-subject means and s.e.m.s. (*B*) *r*-squared values of three multiple regression models as arranged in Fig. 16*A*. All of the data points were located closely to the "tuning similarity factors" axis, indicating that the tuning similarity regressors outperformed the RD and CD regressors in explaining the variance in pairwise correlation when static ambient visual stimuli were constantly provided to the subjects' eyes. Bars and error bars, across-subject means and s.e.m.s from the main experiment (N = 7). (*C*) Squared part correlations of correlated activities in the "fixation with high contrast" condition (two-way repeated measures ANOVA, $F_{8,48}$ = 13.287, $P < 0.001$ for measures × areas; largest adjusted $P = 0.004$ for SF vs. RD, CD, VD in V1, and *P*'s = 0.019 and 0.006 in V2 and V3 for comparisons with OR). (*D*) *r*-squared values for the tuning similarity, and RD and CD regression models in the fixation with high contrast condition. The format is identical to that of Fig. 16*A*. Bars and error bars in *A*,*C*, across-subject means and s.e.m.s from the main experiment (N = 7).

significantly higher for within-area than between-area pairs ($P < 0.001$, paired-sample *t*-test; comparison between the green and magenta symbols for the driven-state condition in Fig. 16*B*). The results were unchanged when both the RD and the RF overlap factor were included in the regression model ($z_{\text{rest}} = \beta_0 + \beta_1 d_{\text{retinotopic}} + \beta_2 d_{\text{Hellinger}} + \varepsilon$; Fig. 18*B,C*). In sum, the results verified the robust and substantial contribution of tuning similarity in explaining the variances among voxel pairs in both resting-state and driven-state correlations.

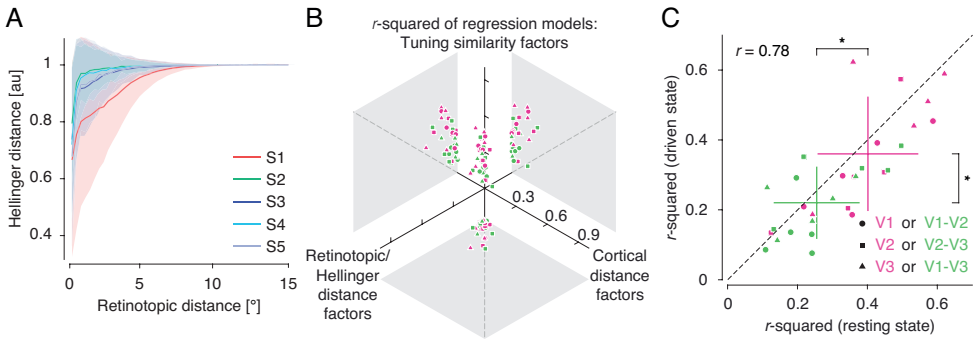

Figure 18. Results from the auxiliary experiment

(*A*) Hellinger distances (HDs) plotted against RDs for individual subjects. The lines and shaded areas are the means and s.d.s across the voxel pairs at around a given RD value. Note that HDs were positively correlated with RDs (0 indicating perfect overlap, 1 no overlap) but varied a lot, particularly in the regime of short RDs. (*B*) Comparisons of the variances explained by the three multiple regression models. The HD measures were included, together with RD measures, as regressors in the model for retinotopic factor (left axis; see text). The format is identical to that of Fig. 8*E*. (*C*) The variances explained by the tuning similarity regression model in the "fixation with high-contrast stimuli" condition were plotted against those in the resting-state condition. The format is identical to that of Fig. 16*C*. Similar to the results from the main experiment, the tuning similarity regressors' contributions to the variances in resting-state and driven-state correlations are highly similar throughout the voxel-pair conditions indicated by different colors and symbols. * for $P < 0.001$, paired-sample *t*-test. Bars and error bars, across-subject means and s.e.m.s from the auxiliary experiment (N = 5).

2.6. Invariance of Stimulus-Tuned Covariability to Changes in Spatial Scale

So far, we have examined the contribution of tuning similarity to resting-state correlation in the pools of voxel pairs residing within a dorsal or ventral quadrant of a given visual area in the same hemisphere. However, if we put aside the CD factor, whose contribution to resting-state correlation turned out to be the smallest compared with the other factors, including VD (Figs. 6, 8, 14*E*), we can expand the pool of voxel pairs beyond those restricted cortical regions. Hence, we examined the predominance of the tuning similarity factors for diverse pools in which voxel pairs are chosen between anatomically noncontiguous subregions, split either between the hemispheres or between the dorsal and ventral parts or both (for a graphical definition of these voxel-pair pools, see the figure legends under "Quadrant pair" in the bottom right of Fig. 19). Consistent with the results described in the previous sections, the squared part correlations of resting-state correlation with tuning similarity for SF (Fig. 19*A*; $P < 0.001$, rank-sum test) and for OR (Fig. 19*B*; $P < 0.001$) were higher than those with RD in the majority of pools of voxel pairs. In addition, most of the squared part correlations with SF

tuning similarity were higher than those with OR (Fig. 19*C*; $P < 0.001$), suggesting the stronger contribution of SF tuning similarity to resting-state correlation compared to that of OR tuning similarity at large scale. Notably, the contribution of tuning similarity to resting-state correlation varied substantially across the pools both for SF (across-pool mean and s.d. of sr^2, 0.117 and 0.071) and OR (mean and s.d., 0.049 and 0.038), whereas the contribution of RD was kept low throughout the different pools (mean and s.d., 0.020 and 0.011). In particular, the contributions of OR to resting-state correlation varied greatly, such that it became similar to or even smaller than the contribution of RD in a few pools (leftward triangles in Fig. 19*B*).

The observed large variability in the tuning similarity's contribution to resting-state correlation could reflect intrinsic differences in anatomical connections for given pools of voxel pairs. Alternatively, however, this variability could arise due to the differences in tuning similarity regime across the different pools. In other words, it is possible that a given pool exhibits a relatively high squared part correlation between tuning similarity and resting-state correlation because the given pool happens to include the voxel pairs with relatively high degrees of tuning similarity. This seems a plausible scenario because, as confirmed in our data (Fig. 2), the distributions of SF preferences differ substantially

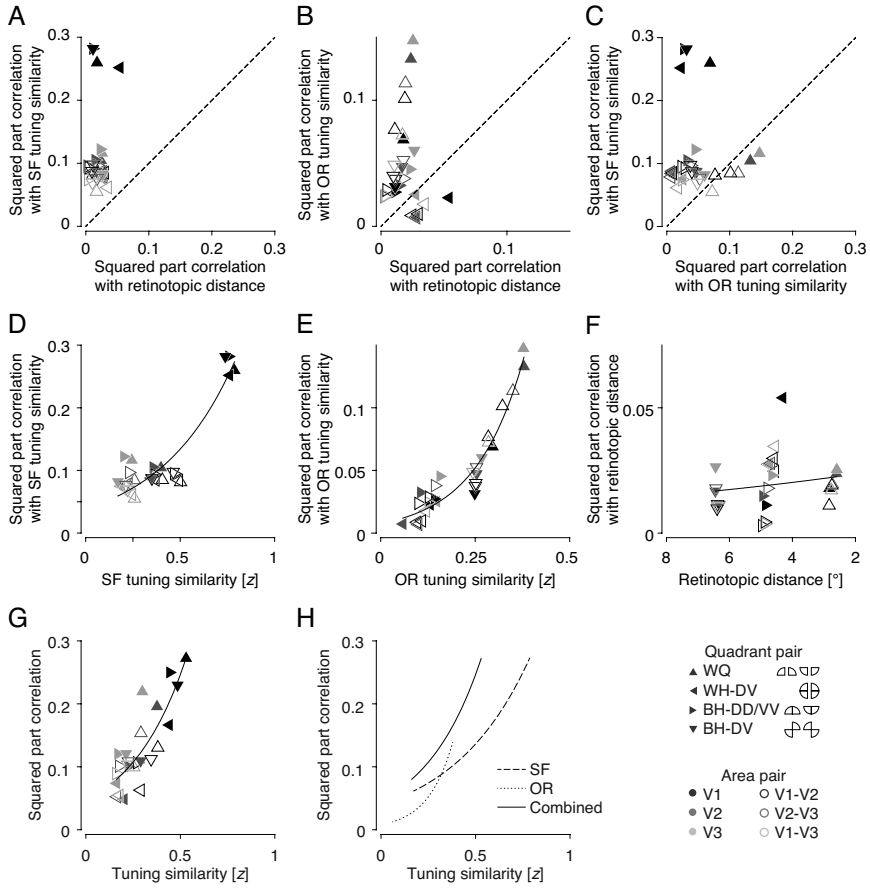

across visual areas (Henriksson et al. 2008) while the OR preferences vary systematically over visual field quadrants (Freeman et al. 2011). Moreover, a close inspection of our own data indicates that the association between tuning similarity and resting-state correlation appears to become increasingly stronger as the regime of tuning similarity among voxels increases, as indicated by the monotonic increase

Figure 19. Stimulus-tuned resting-state correlations from the diverse pools of voxel pairs defined between visual field quadrants or visual areas

(*A*–*C*) Comparisons of the squared part correlations of resting-state correlation with SF (*A*) and OR tuning similarity (*B*) and RD (*C*). (*D*–*F*) The squared part correlations plotted against the median values of tuning similarity in SF (*D*) and OR (*E*), and RD (*F*) for the different pools of voxel pairs. (*G*) The squared part correlations plotted as a function of the combined tuning similarity measure, $\left(z_{\text{tuning}}^{SF} + z_{\text{tuning}}^{OR}\right)/2$. The format is identical to those of *D* and *E*. (*H*) Exponential fit curves shown in *D*,*E*,*G* are plotted together for comparison. (*A*–*G*) Symbols are across-subject means (N = 7) for each area- and quadrant-pair condition, each of which representing 24 non-overlapping pools of voxel pairs. Pools were defined jointly by six area- and four quadrant-pair conditions (see bottom right for legend): WQ for the within-quadrant pairs, WH-DV for the within-hemifield dorsal-ventral quadrant pairs, BH-DD/VV for the between-hemifield dorsal-dorsal or ventral-ventral pairs, BH-DV for the between-hemifield dorsal-ventral quadrant pairs.

in the slope of the exponential fit to the data with an increasing degree of tuning similarity at a given regime (in Fig. 11*A*,*B*).

To verify this possibility, we calculated the median values of tuning similarity of the voxel pairs within the individual pools and plotted those values against the corresponding squared part correlations of tuning similarity with resting-state correlation. First of all, we found that the degree of tuning similarity substantially varied across the pools (across-pool mean and s.d. of tuning similarity: 0.377 and 0.217 for SF; 0.206 and 0.091 for OR; Fig. 20*A*,*B*). More importantly, the median values of tuning similarity were positively correlated with the squared part

correlations for both SF and OR (rank correlation: ρ = 0.574 and P = 0.004 for SF; ρ = 0.943 and P < 0.001 for OR). Consistent with the previous studies (Henriksson et al. 2008; Freeman et al. 2011), the median values of SF tuning similarity tended to vary over the pools along the dimension of visual area (highest in V1 pools; solid dark symbols in Fig. 19*D*), whereas the median values of OR similarity tended to vary along the dimension of visual quadrant (as indicated by the clusters of the same symbols in Fig. 19*E*). These regime-dependent increases in stimulus-tuned correlation were quite robust, being evident when inspected at the level of individual subjects (Fig. 20*D,E*) and also when the two tuning similarity measures for SF and OR were combined into a single metric by taking their arithmetic mean (Fig. 19*G,H*). In contrast, although the median values of RD also varied substantially over the pools as in the case of SF and OR (Fig. 20*C*), but it did not exhibit any systematic relationship with the squared part correlation between RD and resting-state correlation (rank correlation, P = 0.065; Figs. 19*F*, 20*F*). The similar results were obtained when voxel pairs were defined either between the upper and lower vertical meridians or between the left and right horizontal meridians (Fig. 21). Taken together, we conclude that the predominance of tuning similarity over RD as the governing factor of correlated resting-state activity holds even when the voxel pairs are

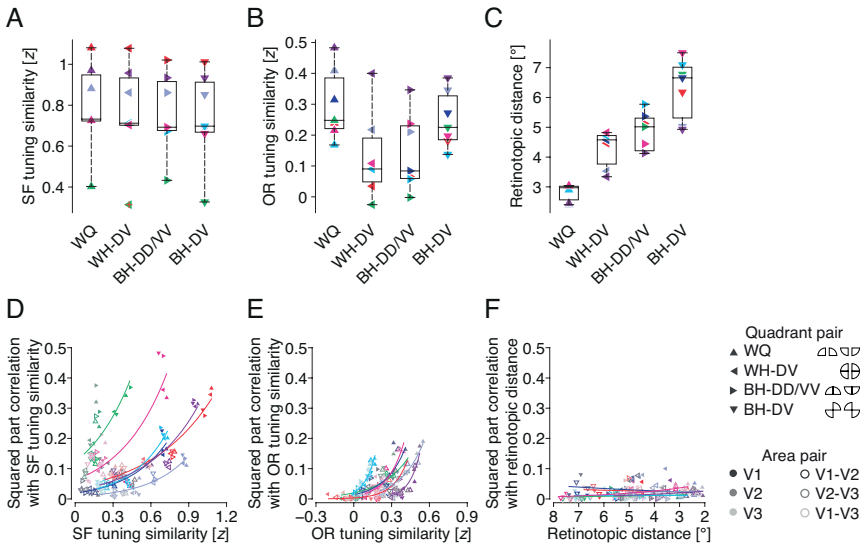

Figure 20. Variability of tuning similarity across visual quadrants and areas, and their relationship with the contributions to the resting-state correlations at the level of individual subjects

To examine how the tuning similarity and RD measures vary across the different visual field quadrants, we plotted the medians of the tuning similarity in SF and OR, and the RD in V1 for the four visual-field quadrant-pair conditions. Different colors represent different subjects. The SF tuning similarity was constant across the quadrant-pair conditions (*A*). The OR tuning similarity (*B*), however, was much lower when voxel pair pool was taken from the adjacent quadrants (WH-DV and BH-DD/VV) than from the same quadrant (WQ), or even from the quadrant pairs most apart (BH-DV). Such trend was clear despite the substantial within-subject variability for both SF and OR tuning similarities (*A,B*). As expected, the median values of RD systematically varied across quadrant-pair conditions (*C*). (*D–F*) Squared part correlations were plotted against the three relational measures. The curves are the exponential fits to the data points for the individual subjects, and the symbols are the 24 possible combinations of the quadrant- and area-pair conditions (inset at the right of *F*). The squared part correlation increased as a function of the median values of the tuning similarity measures (*D,E*), but not of the distance measure (*F*). The data were from the main experiment (N = 7).

defined between anatomically noncontiguous regions, and that the apparent regional variability in predominance arises mainly due to the corresponding variability in the range of tuning similarity.

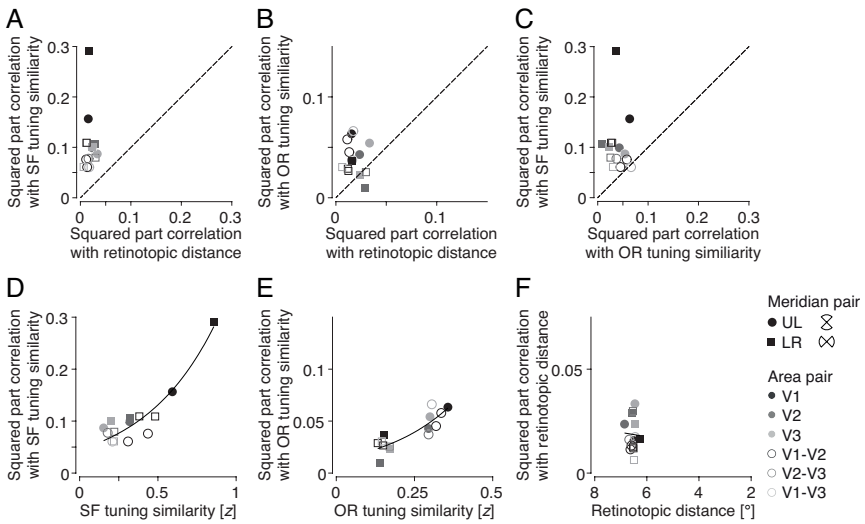

Figure 21. Stimulus-tuned covariability for between-meridian voxels pairs

The same analysis shown in Fig. 19 was applied to the voxel pairs taken between the upper and lower vertical meridians (UL), and between the left and right horizontal meridians (LR). The symbols are the across-subject means for each of the 12 combinations of the meridian- and area-pair conditions (inset at the right of *F*). As found in Fig. 8*A*–*C*, the squared part correlations of the tuning similarity factors with resting-state correlation were larger than those of the RD factor at all the conditions for SF (*A*; $P < 0.001$, rank-sum test), and at the majority of the conditions for OR (*B*; $P = 0.005$). The SF tuning similarity factor was superior to that of OR (*C*; $P < 0.001$). Notably, as previously known, the OR tuning similarity was higher for the UL pairs than for the LR pairs (*E*; $t_5 = 11.221$ and $P < 0.001$, paired-sample *t*-test), whereas no such difference was found for SF tuning similarity (*D*; $t_5 = 1.712$ and $P = 0.148$). The variations of the squared part correlations across the voxel pair pools were readily predicted by the level (median value) of tuning similarity in SF (*D*; $\rho = 0.601$ and $P = 0.043$, rank correlation) and OR (*E*; $\rho = 0.846$ and $P < 0.001$), but not for RD (*F*; $P = 0.749$). The data were from the main experiment (N = 7).

2.7. Spatial Structure of Stimulus-Tuned Covariability

Human subjects' performances in many visual tasks are not spatially homogeneous but vary substantially over the visual field (Hess and Dakin 1997; Liu et al. 2006; Abrams et al. 2012; Anderson et al. 2014). Inspired by this, we explored the possibility that the spatial structure of stimulus-tuned covariability might also vary across visual field locations. To do so, we examined how the contribution of the tuning similarity factors to the resting-state correlations within local voxel pair pools changes along the two major axes of the retinotopic space. The predominance of tuning similarity factors exhibited an intriguing yet systematic pattern of inhomogeneity along both the eccentricity and polar angle axes, particularly when the CD was short (CD less than 20 mm for Fig. 22*A*; thick lines in Fig. 22*B*,*C*). The SF-tuned covariability was prominent at the foveal region of the visual field when inspected along the eccentricity axis (top panel of Fig. 22*A*, and red lines in the bottom panel of Fig. 22*B*), and at the horizontal meridians when inspected along the polar angle axis (top panel of Fig. 22*A*, and red lines in the bottom panel of Fig. 22*C*). On the other hand, the OR-tuned covariability was weakly dependent on the eccentricity (middle panel of Fig. 22*A*, and green lines in the bottom panel

of Fig. 22*B*), but was strongest at the vertical meridian in the low visual field and became weak monotonically as it moved along the polar angle axis towards the upper vertical meridian (middle panel of Fig. 22*A*, and green lines in the bottom panel of Fig. 22*C*). These inhomogeneities of the tuning similarity factors were robustly found across subjects and CD range conditions, and could not be attributed to variability in the fMRI signal noise because the squared part correlation with VD was low and flat across eccentricities and angular positions (bottom panel of Fig. 22*A*, and black lines in the bottom panels of Fig. 22*B*,*C*).

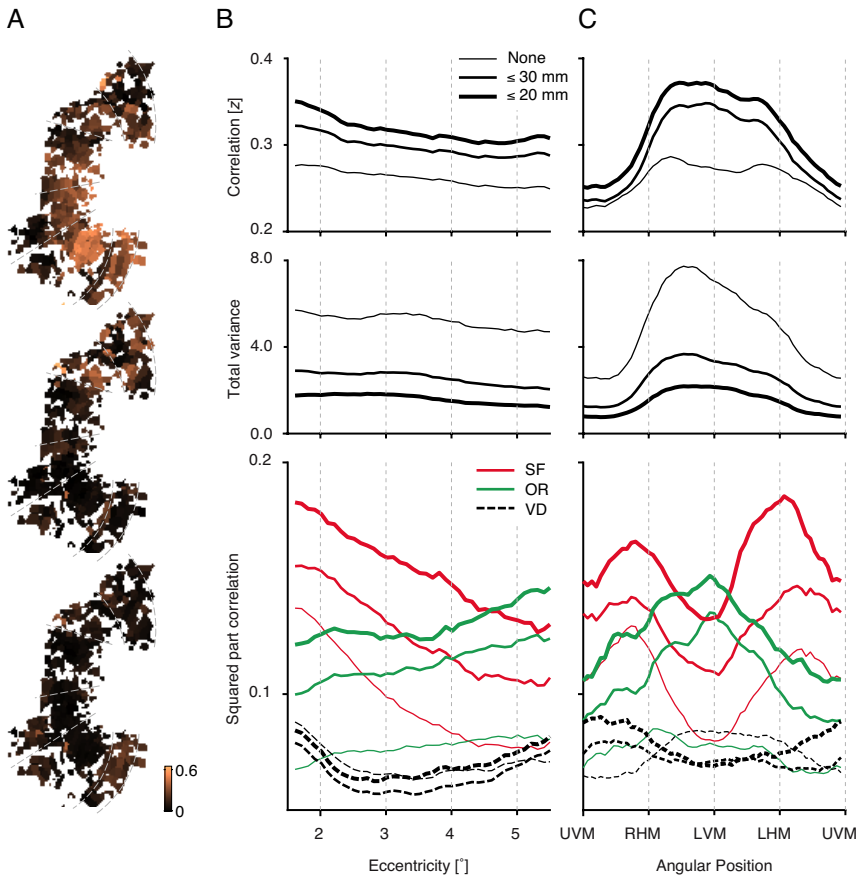

Figure 22. Stimulus-tuned resting-state correlations over space

(*A*) Squared part correlations (computed within a pool with CDs less than 20 mm at each seed voxel) with SF (top) and OR tuning similarities (middle), and VD (bottom) overlaid on a flattened cortical surface. (*B*,*C*) The means (top panels), total variances (middle panels), and explained variances of resting-state correlations (bottom panels), averaged over 7 subjects, plotted against eccentricity (*B*) and angular position (*C*) of the seed voxels. The sizes of sliding bins were ± 1° for eccentricity (B) and ± π/4 for angular position (*C*).

2.8. Stimulus-Tuned Dynamics of Resting-State fMRI Activity

Though previous fMRI studies have reported that resting-state correlations are not constant, but rather change over time (Chang and Glover 2010), the factors responsible for such temporal variations of the structure of resting-state correlation have not been identified. As candidates for such factors, we considered the three relational factors that have been evaluated for the contribution to the structure of correlated resting-state activity in the previous sections. Again, we carried out the same part correlation analysis, but here evaluating how the contributions of the relational factors to resting-state correlation fluctuate over time and how the contributions co-vary between the relational factors within or between visual areas. The detailed procedure is described in below.

First, for each voxel pair, we binned their time series with a sliding time window of 30 s and computed the resting-state correlations across those consecutive bins. As documented in the previous studies mentioned above, the resting-state correlations, when averaged across

voxel pairs, did fluctuate substantially over time (bottom panel, Fig. 23*A*). Then, as previously done in the previous sections (Figs. 8–15, 17), we divided the voxel pairs into anatomically contiguous dorsal and ventral sub-regions within each hemisphere and computed the squared part correlations across the sliding time bins, respectively for those sub-regions (Fig. 23*B*).

In overall, the squared part correlations fluctuated a lot over time, held true for all the relational factors in all the visual areas. Notably, however, the contribution of the tuning similarity in SF to the resting-state correlation in V1 stood out, showing the largest temporal variations, unparalleled by the contributions by any other factors in any other areas (red curves, Fig. 23*B*; red bars, Fig. 23*C*). We also note that the contributions of the OR tuning similarity were relatively larger in V2/V3 than in V1 (green curves, Fig. 23*B*; green bars, Fig. 23*C*). By contrast, the temporal variations of the distance factors' contributions did not differ substantially between the visual areas (dark and light blue curves and bars in Fig. 23*B,C*).

Next, we turn to inspect whether and how the squared part correlations co-fluctuated over time among the relational factors within or between the visual areas. Within the areas, there were no noticeable

coherences between any of the relational factors (Fig. 23*B*). By contrast, coherent fluctuations of the squared part correlations were found between the visual areas, between the spatially contiguous visual areas. For example, the RD-dependent and the CD-dependent resting-state correlations co-fluctuated, waxing and waning in synchrony, between V1 and V2 and between V2 and V3 (left and middle panels respectively in Fig. 23*D*). However, no such between-adjacent-areas co-fluctuation were observed between the tuning similarity factors, SF and OR. Instead, the SF tuning similarity factor was more coherent with the distance factors than the OR tuning similarity factors for the between-area comparisons.

Figure 23. Temporal dynamics of stimulus-tuned covariability in human visual cortex

(*A*) Dynamics of population activity of a single resting-state run. The percent BOLD signals were z-scored for each voxels (upper panel). Population activities averaged across voxels (middle panel). Resting-state correlations averaged across voxel pairs (lower panel). Gray traces represent variance. (*B*) Time courses of squared part correlations for tuning similarity and distance measures, computed from dorsal V1, V2, and V3 (upper, middle, and lower panels, respectively). (*C*) s.d.s of squared part correlations averaged across subjects and runs. Error bars, s.e.m.s. (*D*) Correlations of squared part correlation time courses between relational factors (rows and columns) for V1 and V2 (left), V2 and V3 (center), and V1 and V3 areas (right).

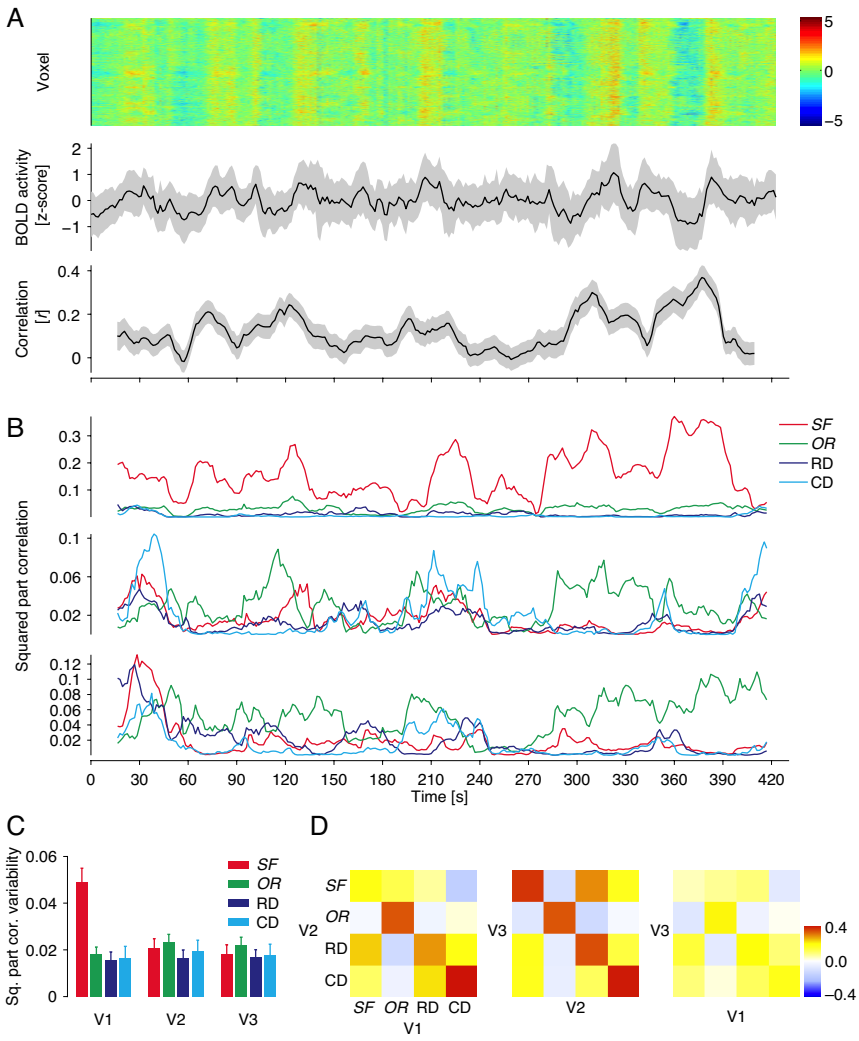
A
Voxel
5
0
−5
BOLD activity [z-score]
2
1
0
−1
Correlation [r]
0.4
0.2
0
B
Squared part correlation
0.3
0.2
0.1
0.1
0.06
0.02
0.12
0.1
0.08
0.06
0.04
0.02
0
30
60
90
120
150
180
210
240
270
300
330
360
390
420
Time [s]
SF
OR
RD
CD
C
Sq. part cor. variability
0.06
0.04
0.02
0
V1
V2
V3
SF
OR
RD
CD
D
V2
V3
V3
SF
OR
RD
CD
SF OR RD CD
V1
V2
V1
0.4
0.0
−0.4

3. DISCUSSION

In the visual system, incoming sensory information is initially encoded in the retina and sent to V1 via parallel hierarchical connections. The local V1 sites receiving those parallel inputs are densely linked with one another via horizontal connections. These hierarchical and horizontal connections toward the local sites in V1 are organized in complicated yet systematic ways to subserve the multitude of representational functions of V1 (Nassi and Callaway 2009). According to the view that spontaneous cortical activity is constrained by intrinsic anatomical connections (Ringach 2009), the spontaneous activity in V1 can be understood as a phenomenon occurring in a multilayered network (Radicchi 2014), where the functional connectivity between nodes, as measured by the correlations between the activities of cortical sites, is affected by the multiple rules by which the anatomical connections are organized. In this perspective, we reasoned that at least three different layers of connectivity comprise the network of the visual cortex.

First, it is possible that the more proximal cortical sites over the retinal surface are more strongly correlated, as the neighboring sites at

the V1 surface are likely to have more shared projections from the retina (Tootell et al. 1988). On the other hand, guided by the anatomical connections within V1 biased toward sites that are spatially close over the cortical surface (Douglas et al. 1995) or similar in stimulus feature preferences (Stettler et al. 2002), it is also possible that the correlated activity depends on the proximity along the cortical surface and the similarity in stimulus feature tuning.

In this study, we evaluated and confirmed the respective contributions of these three connectivity factors to the correlated variability in spatially (2 mm-iso voxel level) and temporally (< 0.1 Hz) large-scale spontaneous activity in the human visual cortex (V1, V2, and V3). Further, our results suggest the robust predominance of the tuning similarity factors over the distance factors in governing the core structure of correlated resting-state activity.

3.1. Predominance of Tuning Similarity over Retinotopic and Cortical Distance

Previous imaging studies on the human visual cortex reported the contributions from RD and CD factors to correlated spontaneous activity for diverse pools of voxel pairs. When the RFs of cortical sites in V1 and V3 were projected onto the retinotopic field, the resting-state correlation of those between-area voxel pairs peaked at around zero distance and decreased gradually as the RD increased (Heinzle et al. 2011). This between-area evidence for retinotopic contribution to resting-state correlation was corroborated by another study (Raemaekers et al. 2014), which inspected the between-hemisphere voxel pairs within the same visual areas. The same study (Raemaekers et al. 2014), on the other hand, also reported the systematic decrease of resting-state correlation with increasing CD for the voxel pairs defined within early visual areas. The dependence of resting-state correlation on CD held true even for the between-hemisphere voxel pairs when their CDs were re-estimated based on each other's proxy (mirrored) site in the opposite hemisphere (Butt et al. 2013). In line with these studies, the resting-state correlation systematically decreased as a function of both RDs and CDs for the voxel

pairs that differed in areas of origin but belonged to the same hemisphere (Gravel et al. 2014). Consistent with these previous studies, RD and CD factors both contributed substantially to resting-state correlation when evaluated with simple Pearson correlation coefficients in the present study (Figs. 3*I,J* and 6*A*; gray bars in Fig. 6*D*).

The present study goes beyond these previous imaging studies by identifying an unprecedented, strong factor that governs correlated spontaneous activity in the human visual cortex, similarity in stimulus feature tuning in SF and OR between local cortical sites. Furthermore, our results provide converging evidence for the predominance of tuning similarity over the distance factors in contributing to the resting-state correlation. First, this was confirmed with three complementary analyses: simple correlation (Fig. 6*A*), part correlation (Fig. 6*C*), and multiple regression (Fig. 16*A*). Second, it was identified not only in V1 but also in V2 and V3 (Fig. 8*A*). Third, it was identified not only for the voxel pairs within the same areas, but also for the pairs comprising voxels located in different visual areas (Fig. 16*A*) and visual quadrants (Fig. 19). Fourth, it was demonstrated not only in the complete absence of visual input but also when visual stimulation was uniform in luminance or when it was richly structured with spatiotemporal contrast variation (Fig. 16*B*). Finally, all of the above findings were replicated both when the

alternative metrics of the RD and tuning similarity factors were applied and when the experiments were repeated for a different pool of subjects using different methods.

3.2. Concurrent Evaluation of Spatial Proximity and Tuning Similarity

The individual sites of primate V1 can be mapped back not only onto the retinal positions of their RFs, but also onto the visual features in the environment that they are tuned to along multiple stimulus dimensions. Each of these "feature" maps exhibits spatially smooth and periodic changes in tuning property over the cortical surface at multiple spatial scales (Hubel and Wiesel 1962; Bonhoeffer and Grinvald 1991; Henriksson et al. 2008; Kara and Boyd 2009; Freeman et al. 2011; Nauhaus et al. 2012). Owing to this overlay of feature and retinotopic maps onto the cortical surface, the neighboring sites on the cortical surface (CD factor) of V1 are more likely to respond to nearby points on

the retinal surface (RD factor), and they also share similar tuning properties in multiple feature dimensions (tuning similarity factor). In our data, this interdependence of the three relational factors was evidenced by the high correlation coefficients among those factors (Fig. 6*B*). With the presence of this interdependence, the explanatory power cannot be correctly estimated by measuring a single explanatory variable of interest alone (Fig. 7*C*). To overcome this limitation, we acquired RD, CD, and tuning similarity measures together, which were estimated by independent experiments or analyses, and then evaluated their individual and unique contributions to correlated resting-state activity by computing the part (semi-partial) correlation. By this approach, we showed that the contributions of the RD and CD factors to correlated spontaneous activity become reduced substantially (over 5 pp reduction; Fig. 6*D*) when those factors' correlations with the tuning similarity factors were controlled. This suggests that the contributions of the RD and CD factors that have been reported in previous studies were likely to be a mixture of their own contributions and joint contributions with the tuning similarity factors.

Recently, it was reported the augmented degrees of resting-state correlation for between-area voxel pairs whose RFs fall at similar eccentricities (Yeo 2011; Arcaro 2015; Butt 2015) or at similar radial

angles (Arcaro 2015). If these findings are taken together with the well-known associations between SF similarity and eccentricity distance and those between OR similarity and angular distance (Fig. 2*G*; Henriksson et al. 2008; Freeman et al. 2011), one may assert that the observed contribution of tuning similarity to resting-state correlation is spurious and can be explained by spatial biases in resting-state correlation along the polar-coordinate axes of retinotopic space. Wielding the part correlation method again, we directly rejected this assertion by pitting those eccentricity and polar-angle distance measures against the SF and OR similarity measures, respectively, to explain the variance of resting-state correlation across voxel pairs (Fig. 6). This overriding dominance of the tuning similarity factors over the polar-coordinate distance factors (as illustrated in Fig. 14*B,C*) is worthy of special note, particularly when considering their large-scale associations with one another (e.g., the SF/OR tuning similarity and the eccentricity/angular position difference maps in Fig. 14*A* look quite similar on a large scale, but exhibit subtle yet substantial differences on a fine scale as well). This indicates that the patterns of the correlations in BOLD fMRI activity in visual cortex indeed carry reliable and substantial information about fine-grain population neural activities representing stimulus features that cannot be simply reduced to obtuse blurring of underlying neural signals.

Based on these findings and analyses, we conclude that, although the distance factors contribute to resting-state correlation via multiple routes over the retinal or cortical surface, their contributions were minimal when their correlation with the tuning similarity factors was controlled. In a series of control analyses and experiments (Fig. 8*C,E*; Figs. 12–15), we also showed that the predominance of tuning similarity over distance factors is unlikely to be ascribed to the possible suboptimality or unfairness in our definition of distance or similarity measures for the relational factors.

On a cautionary note, we remark that our findings, like any other outcomes of correlational analysis, should be taken as a demonstration of the tuning similarity factors' strong association with, not their causation of, resting-state correlation. Furthermore, the part correlation effectively isolated the shared variance between the tuning similarity factors and the distance factors, but it does not provide information about the source of that shared variance. Indeed, the retinotopic organization may give rise to the stimulus tuning properties of the visual cortex via intricate and sophisticated spatial arrangements of the thalamic projections from the retina (Kremkow et al. 2016). We also recognize that, although the two tuning similarity factors we identified in the current study, SF and OR, alone explained a substantial fraction (> 30 pp) of the total variance of

resting-state correlation, other unexplored factors still might account for the variance further, such as stimulus tunings in other visual features, cross-callosal anatomical connections and vascular structures.

3.3. Implications for Optimal Population Decoding

Recent advances in theoretical neuroscience provides a formalism that enables determination of how read-out weights of encoding stage neurons should be assigned for optimal decoding, depending on how they are correlated (Haefner et al. 2013). Despite its computational elegance, there is a practical hurdle for application of this formalism to empirical data; specifically, it requires both a complete noise correlation matrix and a stimulus tuning matrix for the entire sensory neural population, both of which are difficult to obtain, particularly in electrophysiological studies on animals. The results presented here provide an opportunity to empirically deduce optimal decoding weights because comprehensive matrices of signal responses and noise correlations were generated for a cortical region representing an extended and balanced region of the

visual field. To explore the decoding consequences of the stimulus-tuned covariability identified here, we performed a simulation where the covariance matrix was derived from the regression of correlated activity onto tuning similarity (Fig. 24), and subjects were engaged in a discrimination task on different visual stimuli. The simulation results indicate that the optimal decoding weights should be determined not only by the tuning curves of the neurons at the encoding stage but also by the interaction between the trial-by-trial correlations among them and visual targets to be discriminated (Abbott and Dayan 1999; Chen et al. 2006; Estebanez et al. 2012). This implies that the neural system would be suboptimal in perceptual decision making without taking into account the relationship between tuning similarity and noise correlations (Beck et al. 2012).

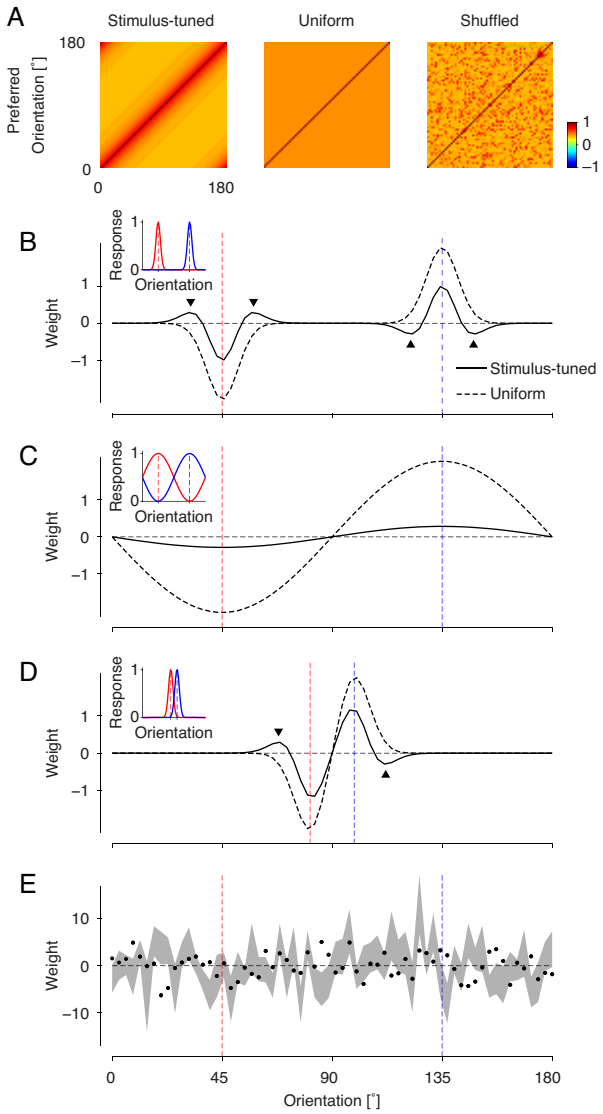
A
Stimulus-tuned
Uniform
Shuffled
Preferred Orientation [°]
180
0
0
180
1
0
−1
B
Response
Orientation
Weight
Stimulus-tuned
Uniform
C
D
E
10
−10
0
45
90
135
180
Orientation [°]

Figure 24. Optimal decoding weights prescribed by stimulus-tuned covariability

(*A*) Matrices of noise correlations between 64 simulated neurons with orientation preferences. The exponential regression on OR of the resting-state correlations from a representative subject was used in the left panel, its mean in the middle panel, and its randomly shuffled values in the right panel. (*B,C,D*) Optimal decoding weights for stimulus-tuned and uniform correlation matrices. We considered three different task situations, in which subjects discriminated two sharply oriented stimuli centered around an orthogonal pair of orientations (inset in *B*), two broadly oriented stimuli centered around an orthogonal pair of ORs (inset in *C*), or two sharply oriented stimuli whose centers were located close to each other (inset in *D*). Solid and dashed black curves, decoding weights for stimulus-tuned and uniform correlations, respectively. Colored curves in the insets denote population response profiles to two stimuli (red and blue), centered at the locations indicated by dashed vertical lines. The vector of optimal decoding weight, w, was approximated with the following formula (Haefner et al., 2013), $w = \boldsymbol{C}^{-1}[r_r - r_b]$, where $\boldsymbol{C}$ is the correlation matrix (shown in *A*), r_r and r_b are the population response profiles to the two stimuli indicated by the red and blue (shown in the insets in panel *B,C,D*). When the uniform correlation matrix was applied, the profiles of the decoding weights were always scaled copies of the differences between the population response profiles (dashed black curves). However, when the stimulus-tuned correlation matrix was applied, the profiles of the optimal decoding weights (solid black curves) deviated substantially from or were similar to those of the uniform correlation matrix, depending on how broad the population responses to the stimuli were. When the population response profiles were broad, the optimal weight kernel resembled a scaled copy of the difference between two population responses (solid line in *C*). By contrast, when the population response profiles were narrow, the weights for neurons whose preferred orientation flank those of neurons that were driven maximally by the stimuli had opposite signs to those for the other neurons in the sample decision pool (*B* or *D*). (*E*) Optimal weights for decoding the stimuli in b with the shuffled correlation matrix. Black dots, example weights associated with the shuffled correlation matrix shown in a. Gray shaded area, mean and s.e.m. of the weights from 100,000 simulations based on different shuffled matrices. When the shuffled correlation matrix was applied, the decoding weights were not smooth and were highly variable across the shuffled samples, suggesting the destructive decoding consequences of out-of-tune covariability.

3.4. Origin of Mesoscopic Stimulus-Tuned Covariability

The origin involved in the systematic and robust stimulus-tuned covariability observed in this study is currently unknown. One explanation may be offered by the Bayesian perspective on spontaneous brain activity (Berkes et al. 2011), in which neural activity in the sensory cortex is conceptualized to reflect the inferred probability that a particular set of features causes sensory inputs. In this framework, spontaneous cortical activity in the visual cortex mirrors the prior knowledge of the co-occurrence statistics of visual features in the environment. Several aspects of our findings are consistent with this conjecture. First, the SF-tuned covariability and the OR-tuned covariability in V1 were both dependent on RD (Fig. 6*E*), albeit differing in degree, suggesting that the spontaneous activities tuned to similar visual features are strongly correlated when their RF positions are close rather than apart in the visual field. This is consistent with the findings that the co-occurrences of the same OR edges reflect the co-circular

geometry in natural image statistics (Sigman et al. 2001) and are limited to a short distance range (< 1.5°) (Geisler et al. 2001). Similarly, the SF, capturing a large-scale visual feature (Oliva and Torralba 2001), also changes gradually over space (Simoncelli and Olshausen 2001). Moreover, the robust invariance of the stimulus-tuned covariability to the subjects, visual areas, local pools of voxel pairs, and viewing conditions is consistent with the notion that prior knowledge about the visual environment is shared widely across the population, irrespective of stimulation regimes.

There is an intricate resonance between recent animal studies and ours, despite substantial differences in spatiotemporal scale. The stimulus-tuned covariability in the present study was carried by BOLD signals, which are strongly associated with local field potential activity in the range of slow cortical potentials (0.01–5 Hz) (Lu et al. 2007; He et al. 2008) or electroencephalography activity in the infra-slow range (0.01–0.1 Hz) (Vanhatalo et al. 2005; Chan et al. 2015). In line with this, the large degree of cofluctuations in our data also arises at less than 0.1 Hz (Figure 5*B*). However, many animal studies have also found that the neural covariability at high temporal frequencies depends on stimulus tuning similarity (Ts'o et al. 1986; Gray et al. 1989; Zohary et al. 1994; DeAngelis et al. 1999; Maldonado et al. 2000; Smith and Kohn 2008;

Jermakowicz et al. 2009; Ch'ng and Reid 2010; Ko et al. 2011; Denman and Contreras 2014). It has been suggested that this may reflect the dynamics of the intrinsic modular networks (Mohajerani et al. 2013) that are specific to stimulus features (Miller et al. 2014; Kiani et al. 2015; Romano et al. 2015).

Given the strong contributions of tuning similarity factors both on a fine scale, as evident in animal studies (Chu et al. 2014; Schulz et al. 2015), and on a coarse scale, as demonstrated in the present study, we speculated about the possible mechanism-level determinants and functional consequences of stimulus-tuned covariability that can be shared by neural activities occurring at various spatiotemporal scales. For one of those possibilities, we conjecture that the stimulus-tuned structure of correlated fMRI activity in our data may be substantiated by a mechanism that mediates cross-frequency coupling or entrainment, which extends up to 200 Hz and down to 0.01 Hz (Lakatos et al. 2005; Canolty et al. 2006; Lakatos et al. 2008) and is coupled with the infra-slow phase changes in performance on visual detection tasks (Monto et al. 2008). In line with this possibility, it was recently proposed that the statistical features of population neural activities at high temporal scales may give rise to the skewed (with a heavy tail or log-normal) statistical distributions of oscillatory cortical activities at mesoscopic or

macroscopic scales or even of various perceptual or cognitive behaviors (Buzsáki and Mizuseki 2014). Intriguingly, according to this proposal, the augmented stimulus-tuned structure of resting-state correlation among voxel pairs with high degrees of tuning similarity (Fig. 19*D,E,G,H*; Fig. 20*D,E*; Fig. 21*D,E*) suggests that a "rich club," a minority of cortical sites sharing a bulk of information with strong mutual connectivity (van den Heuvel and Sporns 2011), exists in the functional network of the human visual cortex, and that the membership to that rich club appears to be ruled by tuning similarity. Given the many functional and computational roles ascribed to a rich club organization (Sporns 2010; Buzsáki and Mizuseki 2014), investigating the behavioral consequences of the stimulus-tuned covariability in the early visual cortex that is structured both space and time we found (Figs. 22, 23) surely will be one of the exciting topics for future studies.

4. MATERIALS AND METHODS

4.1. Subjects

The study included seven human subjects (six men) aged between 21 and 37 years who had normal or corrected-to-normal visual acuity. Written informed consent was obtained from each participant, and the experiments were performed in compliance with the safety guidelines for MR research, as approved by the Institutional Review Board of Seoul National University. Each subject participated in three scanning sessions: one for imaging whole brain anatomy and retinotopic mapping, another for mapping SF tuning, and a third for mapping OR tuning.

4.2. Display

The stimuli were presented by an LCD projector (Canon XEED SX60; Canon) at its native resolution (1,400 × 1,050 pixels; refresh rate, 60 Hz) onto a rear projection screen placed inside the magnet bore. The distance to the screen from the eyes was 87 cm, and the projection area on the screen was 34.5 cm × 26 cm, resulting in a visual angle of 22° (width) × 17° (height). Subjects viewed the stimuli through the front surface of a mirror with a multilayer dielectric reflective coating (Sigma Koki) that was mounted on the head coil. A custom-made neutral density filter (9% transmission rate; Taeyoung Optics) was inserted between the projector lens and the screen to control the overall level of stimulus luminance. The color lookup table was calibrated to linearize the luminance values at the screen center ranging from 0.0045 cd/m^2 to 63.5 cd/m^2 by using a luminance meter (LS-100; Konica Minolta Sensing) in conjunction with in-house software for automated measurement and correction.

4.3. MRI Scanning

Data were collected using a 3 Tesla Siemens Magnetom Trio. The scan parameters for T1-weighted anatomical images (32 channels; MPRAGE) were as follows: repetition time (TR), 1.9 s; time to echo (TE), 2.36 ms; flip angle (FA), 9°; voxel size, 1 × 1 × 1 mm^3; matrix size, 256 × 256. Functional scan data were collected with a 20-channel receive coil from the 24 slices orthogonal to the calcarine sulcus using an EPI protocol with the following parameters: TR, 1.5 s; TE, 30 ms; FA, 75°; voxel size, 2 × 2 × 2 mm^3; matrix size, 96 × 80; GRAPPA acceleration factor, 2; an interleaved slice acquisition order with an interslice interval of 62.5 ms.

4.4. Measurements During Resting State

Each scan lasted either 243 s or 432 s, with the projector lens blocked physically for maintaining a minimum light intensity. The 21 resting-state

scans were administered in 16 (5 and 7 sessions for mapping SF and OR tuning respectively, 4 sessions for retinotopic mapping) out of 21 sessions total, resulting in 3 scans per subject. In the sessions in which resting-state scans were included, the resting-state data were always collected at the beginning to eliminate any possible effects caused by visual imagery and adaptation.

4.5. Preprocessing

The preprocessing procedures were arranged to minimize the factors that can artificially alter the underlying temporal correlations between adjacent cortical locations. First, to avoid the excessive spatial interpolation associated with corrections for within-scan head motions, the slice positions and orientations were updated at every image acquisition (Thesen et al. 2000). After correction of the measurement times for individual slices, the scan data from all sessions were co-registered to the first resting-state scan. The time series were then converted into percent signal changes by subtracting and dividing by the

means for individual voxels. The slow non-physiological baseline activity components (Cordes et al. 2001) were detrended as follows: First, the mean-normalized time series were convolved with a boxcar function with 128 s duration for individual voxels, and then the convolved time series were subtracted from the raw ones. To avoid instigating artificially correlated or uncorrelated activities, additional filtering, such as global signal regression (Murphy et al. 2009), was not performed. In-house analysis codes were used in conjunction with the statistical parametric mapping software SPM 8 (http://fil.ion.ucl.ac.uk/spm) (Friston et al. 1996; Ashburner and Friston 1997) and the mrTools analysis package (http://cns.nyu.edu/heegerlab/?page=software).

4.6. Procedures for Retinotopic Mapping

The boundaries between V1, V2, and V3 visual areas were defined by analyzing the temporal phases of fMRI responses to expanding or contracting rings and rotating wedge stimuli (Engel et al. 1997). To estimate the retinotopic positions for individual voxels, the phase values

were then converted into the positions in radial and angular axes in the visual field (Fig. 4*A*). To improve the reliability of the estimation, the raw time courses of individual voxels were spatially smoothed within each image frame using a surface-based smoothing algorithm (Chung et al. 2008) (Fig. 4*F*). The voxels were discarded when the differences between phases from the raw and the smoothed time courses were $\sqrt{2}$ angular deviations away from the mean differences (Berens 2009). Note that the smoothed time series were used only for the purpose of voxel selection, and that the eccentricities and angular positions were estimated from the raw time series (Fig. 4*G*; see ***Voxel Selection*** below for the other criteria for determining valid voxels).

Black and white dartboard stimuli were presented within ring and wedge apertures, while everywhere else remained the mean gray background. While subjects fixated on the center of the screen, the wedge aperture spanning 45° in the angular direction rotated continuously either clockwise (CW) or counterclockwise (CCW) at a constant speed of 13.3 °/s. The ring aperture spanning 1° in eccentricity either contracted toward or expanded from the center of the screen at a constant speed of 0.296 °/s. Only for two subjects, the ring aperture moved at a speed of $3.64/(30.38 - t)$ °/s, where t is the time from the beginning of each cycle, so that the temporal phase of the ring is approximately proportional to

the log value of (1 + eccentricity). In this case, temporal phase values were first estimated in radians and then converted to eccentricity values in visual angle degree prior to correlation analyses. Stimuli were repeatedly presented for nine cycles per scan, and each stimulus type was repeated twice. The eccentricities and angular positions of the voxels were estimated by averaging the temporal phases of fMRI activities locked to the stimulus frequency (1/27 Hz) across the opposite moving directions of the rings and wedges, respectively.

The phase estimations for the eccentricity mapping may be unreliable because the fixation targets (see below) shaded a small area at the center of the screen, or the responses to foveal and peripheral ring stimuli could spill over to each other because the foveal and peripheral stimuli were presented consecutively in time. To get around these problems, we discarded voxels that responded to the ring stimuli with phases within $\pm\pi/4$ around the phases of the aperture's onset at the screen center. Our procedure resulted in the maximum eccentricity value of 7.0˚ in the scans with the linear-scale eccentricity-mapping stimuli and that of 5.7˚ in the scans with the log-scale stimuli.

4.7. Fixation Task

Except for the resting-state scans, subjects fixated on a stationary red dot (0.14° in diameter) at the center of the screen. To help fixation and control for attention, subjects were asked to press a response button (Current Designs) whenever an opposed pair of tiny (diameter, 0.07°) green dots changed rotation direction (CW or CCW) along a red annulus (width, 0.07°; radius, 0.165°) around the fixation dot. To make the times for the direction change unpredictable, the interval between direction changes was stochastically drawn from a Poisson distribution with a mean of 2 s.

4.8. Procedures for Mapping Stimulus Tuning

While fixating on the screen center, subjects viewed flickering patches of filtered white-noise images. The filters for the SF and OR stimuli

partitioned the identical Fourier space into 18 radial and angular discrete bins, covering 0.2–1.2 cycles/° and 0°–180°, respectively. During presentation, the filter bands changed gradually along the radial or angular axis in Fourier space. To avoid unwanted abrupt changes in the successive filters, the SF filter bands moved in one direction during the first half of the cycle, and in the opposite direction during the second half of the cycle (resulting in first increasing and then decreasing SF, or vice versa). The OR filter bands always moved in a single direction (resulting in CW or CCW rotations).

Visual stimuli. First, random dot image matrices (1,050 pixels × 1,050 pixels) were generated, with the intensities of each pixel independently sampled from the standard normal distribution. Next, the pedestal images were Fourier transformed into an amplitude spectrum, to which we applied two sets of bandpass filters, one defined along the SF axis (0.2–1.2 cycle/°) and the other along the OR axis (0–180°). The filters (Butterworth, order 10) were designed as 18 evenly split bands without overlap between cutoff frequencies. The filtered amplitude spectra were inverse-Fourier transformed back into image matrices. The root-mean-square contrasts of the resulting filtered images were 10.2 ± 0.004 percentage points (pp; mean ± s.e.m. across images; N = 108) for SF stimuli and 12.2 ± 0.19 pp (N = 54) for OR stimuli. Finally, to make the

stimuli outside 8° of eccentricity fade smoothly, we applied a sigmoidal spatial filter, so that SF and OR stimuli span roughly within a disk of 16° in diameter. Visual stimuli were generated using Matlab 2011b (MathWorks) and MGL 1.5.4 (http://justingardner.net/mgl) on an Apple Macintosh OS X computer.

Experimental procedure. Within the 1.5 s time frame assigned to both the SF and the OR filters, the images were updated every 0.25 s with six different image variants to minimize any unwanted adaptation, expectation, or memory effects. These images were generated by applying the same bandpass filter to three independent random dot pedestals, each of which had its own variant with contrast polarity flipped. For the "SF tuning" scans, the 18 SF filter bands gradually changed. In one type of scan (increasing-to-decreasing scan; ID scan), the SF of the filters increased during the first half of a cycle and then decreased during the last half. Each SF band was fixed for 1.5 s, resulting in 54 s for a cycle (36 SF band steps × 1.5 s). Five cycles were repeated per scan. In the other type, the SF first decreased from high to low frequency and then increased back (DI scan; same cycle time and repetitions). In the "OR tuning" scans, the 18 OR filter bands changed gradually in either a CW (starting from the OR parallel to the horizontal meridian, i.e., 0° to 170°) or CCW (opposite sequence to CW scans)

direction. The same sequence was repeated nine times per scan. There were five CW and CCW scans, and three ID and DI scans in each session. The first cycle in each stimulus tuning scan was excluded from data processing. Note that identical sets of images were used repeatedly throughout all of the cycles in the entire session, so that across-cycle or across-scan variability in fMRI signals, if any, cannot be attributed to changes in visual stimuli.

Stimulus tuning similarity. The estimation of stimulus tuning similarity was started by computing the across-cycle average responses of individual voxels, $S(t)$, for each scan type (ID, DI, CW, and CCW) as follows:

$$S(t) = (\overline{x_1}, \overline{x_2}, \cdots, \overline{x_K}), \text{ where } \overline{x_k} = \frac{1}{M}\sum_{m=1}^{M} x_k^m,$$

where x_k^m is the raw fMRI measurement at k^{th} time frame from m^{th} cycle in percent unit, and K is the number of frames per cycle, and M is the total number of cycles. $K = 36$ and $M = 12$ (3 scans × 4 cycles/scan) in the SF tuning scans, and $K = 18$ and $M = 40$ (5 scans × 8 cycles/scan) in the OR tuning scans. Then, Pearson's r values were computed between $S(t)$s for each scan type: r_{tuning}^{ID}, r_{tuning}^{DI}, r_{tuning}^{CW}, and r_{tuning}^{CCW}. The tuning similarities in

SF and OR were defined as the averages of these *r* values, after Fisher's *z* transformation (Fisher 1921):

$$z_{\text{tuning}}^{\text{SF}} = \frac{1}{2}\{F(r_{\text{tuning}}^{\text{ID}}) + F(r_{\text{tuning}}^{\text{DI}})\};$$

$$z_{\text{tuning}}^{\text{OR}} = \frac{1}{2}\{F(r_{\text{tuning}}^{\text{CW}}) + F(r_{\text{tuning}}^{\text{CCW}})\},$$

where $F(r) = \tanh^{-1}(r)$.

4.9. Correlated Variability in Resting- and Driven-State Scans

The correlated variability during the resting-state scans was measured by Pearson's correlations between the raw time series of percent change, $R(t)$s:

$$r_{\text{rest}}^{n} = \text{Cor}\left(R_i^n(t), R_j^n(t)\right),$$

where *n* is the scan number.

After having identified the stimulus-driven components, $S(t)$, from the raw response time series for each stimulus type as described above, we defined the moment-to-moment fluctuations, $D(t)$, by subtracting $S(t)$ from the raw responses as follows:

$$D^m(t) = (e_1^m, e_2^m, \cdots, e_K^m),$$

where $e_k^m = x_k^m - \overline{x_k}$, and m denotes the cycle number within a scan. Note that each cycle within a scan was treated individually, so that each voxel has 104 vectors of $D(t)$s. Then, the correlated variability for the driven-state scans was defined as:

$$r_{\text{driven}}^m = \text{Cor}\left(D_i^m(t), D_j^m(t)\right).$$

The final estimates of the correlated variability in the resting-state and driven-state activities were given respectively by:

$$z_{\text{rest}} = \frac{1}{N}\sum_n F(r_{\text{rest}}^n) \text{ and } z_{\text{driven}} = \frac{1}{M}\sum_m F(r_{\text{driven}}^m),$$

where N is the number of scans, and M is 104, the total number of cycles.

4.10. Voxel Selection

Unusually large fluctuations in fMRI activity are likely to arise from the draining veins (Menon et al. 1993; Lee et al. 1995) and hamper the spatial specificity of signals from nearby tissues (Olman et al. 2007; Shmuel et al. 2007). Thus, we screened out the voxels whose average standard deviations (s.d.) during the resting state were within the largest 20% for each subject (Fig. 4*B*). Next, the remaining voxels were characterized by the multiple stimulus dimensions for retinotopic mapping and stimulus tuning. To avoid any stimulus type (SF or OR) bias in voxel selection, we chose a subset of voxels that were highly responsive to the simple on-/off-stimulation (3 s on and 24 s off) of whole-field visual patterns, the pedestal images of which changed dynamically in SF and OR. The visual stimuli were created by super-positioning two anti-phasic spiral patterns whose pitches varied over time. This configuration was chosen because it creates dynamic changes in the SF and OR energies at any locations in the visual field. The signal-to-noise ratio (SNR) was defined for each voxel in a Fourier domain as the amplitude of the stimulus frequency component (1/27 Hz) divided by the average amplitude of frequency components three times higher than the stimulus frequency. Voxels with SNRs smaller

than two (Fig. 4*C*) were discarded. Voxels that showed anti-phasic activities at stimulus frequency (Fig. 4*D*) were also discarded. The only voxels used in subsequent analyses were those satisfying all criteria set by retinotopic mapping (see ***Procedures for Retinotopic Mapping***) and by on-/off-stimulation, which comprised 42.6% of the total voxels in the regions of interest (1,216.1 ± 85.1 voxels per subject; mean ± s.e.m.; Fig. 4*E*,*H*).

This conservative set of criteria was adopted to ensure the high fidelity of stimulus tuning estimates. However, these criteria are somewhat arbitrary and may limit the generalizability of our findings. Thus, four additional sets of criteria were created and used in control analyses (Fig. 10). The number of valid voxels was slightly increased by relaxing the criteria either for s.d. or for SNR in the first two sets. In the third set, the number of valid voxels was further increased by retracting the criteria not only for s.d. and SNR but also for retinotopic mapping. All voxels were used in the last set by applying none of the criteria.

4.11. Cortical Distance

Previous methods typically measured CD as the vertex-to-vertex distance along a surface mesh, and the vertices were determined by direct distances in an arbitrary direction from the locations of interest, i.e., voxels in functional scans. Here, relying on the known columnar structure of functional units in the visual cortex (Hubel and Wiesel 1962), we computed the CD between voxels by defining a virtual cortical column for each voxel and then measuring the between-column distances. When reconstructing surfaces from anatomical images using FreeSurfer 4.5 software (http://surfer.nmr.mgh.harvard.edu), gray matter (pial) surfaces were reconstructed by iteratively displacing the vertices of the triangularly tessellated white matter surface to the gray matter surface along the direction of the steepest image intensity gradient (Dale et al. 1999). As a result, such repulsive deformation forms vectors orthogonal to the local white matter surface, connecting a white matter vertex to a corresponding gray matter vertex. We defined such a vector as a virtual cortical column at that location. The column that belongs to a voxel of interest was defined by searching for the columns with the smallest projection length from the voxel. Having identified two columns c_i and c_j

for voxels i and j, respectively, we categorized the columns into either a "GM-close" or "WM-close" type based on the distances from each voxel to the gray and the white matter vertices of the corresponding columns. Then, the final estimate of CD was determined by the following rule:

$$d_{\text{cortical}}\,[\text{mm}] = \begin{cases} d^{G}_{\text{cortical}}, & \text{if both } c_i \text{ and } c_j \text{ are GM-close types} \\ d^{W}_{\text{cortical}}, & \text{if both } c_i \text{ and } c_j \text{ are WM-close types} \\ \left(d^{G}_{\text{cortical}} + d^{W}_{\text{cortical}}\right)/2, & \text{otherwise,} \end{cases}$$

where d^{G}_{cortical} is the shortest path lengths between the gray matter vertices of c_i and c_j, and d^{W}_{cortical} between the respective white matter vertices (Dijkstra 1959).

4.12. Part Correlation

A spurious correlation can arise between two variables (X and Y) when they are both correlated with another variable (Z). This problem can be statistically controlled by calculating a part correlation (Abdi 2007), which measures the linear relationship between X and Y after separating

out the influence of Z on Y. This method computes Pearson's correlation between X and R, where R is the residual obtained after Z is linearly regressed out from Y. Thus, in general, the squared part correlation can be interpreted as the proportion of the total variance in X explained solely by Y in the presence of Z. A part correlation, also known as a semi-partial correlation, is different from a partial correlation and has an important advantage: the denominator in the squared part correlation (the total variance in X) remains the same, unlike that for a partial correlation, no matter which variables are being examined (Fig. 7). Hence, the part correlation allows for quantification and direct comparisons of the unique contributions of explanatory variables to a response variable, even when explanatory variables are correlated with one another.

4.13. Procedure and Data Analysis of Auxiliary Experiment

To control for alternative interpretations of our findings, we performed a separate experiment and analyzed the data using complementary methods for RD and the stimulus tuning similarity measures. The major differences between the main and auxiliary experiments were (i) the usage of population receptive field (pRF) estimation methods, (ii) the procedure for mapping SF tuning, and (iii) the voxel selection criteria.

General organization of the experiment and data analysis. Five subjects (aged between 24 to 35 years; four females; one male participated in both the main and auxiliary experiments), who all gave informed consent, participated in three fMRI sessions (experimental protocol approved). Visual areas were localized using the ring and wedge stimuli at the first session. We included the stimulus tuning scans as well as the resting-state scans together in the second session. The advantages of this configuration are that any additional spatial resampling, such as reslicing, other than the within-session motion correction, is unnecessary,

and that this configuration can minimize unwanted day-to-day variations of physiological conditions between the resting-state measurements and both types of stimulus tuning scans. The pRF mapping scans were conducted in the third session. To avoid spatial resampling, we defined the pRFs of voxels in the resting-state scans by searching for the nearest voxels in the pRF mapping scans after co-registration (Park et al. 2013).

Scan protocols. For the localization, stimulus tuning, and resting-state scans, the EPI protocol and slice prescriptions were the same as those used in the main experiment. For the pRF mapping scans, a zoomed-EPI protocol (18 slices with 0.5 mm gap; parallel to the calcarine sulcus; TR, 1.5 s; TE, 37 ms; FA, 75°; voxel size, 2 × 2 × 2 mm^3; matrix size, 128 × 32) was used with a 12-channel head coil.

Estimation of pRFs using moving bar stimuli. Detailed information has been described previously (Park et al. 2013), and here we briefly report the procedures. While fixating on the screen center, subjects viewed the high contrast dartboard patterns presented within an elongated rectangular-shaped aperture of 3° width. The aperture drifted over a distance of 20° at a constant speed (1 °/s) in a single direction

orthogonal to its axis, and a uniform gray stimulus was inserted for 7 s at the end of each cycle. Across eight successive scans, the aperture bar changed its moving direction from 0° (from right to left) to 315° (from right bottom to left top), with an interval of 45° between successive scans. The hemodynamic impulse response functions were estimated for individual subjects from the responses to the on/off whole-field visual stimuli identical to those used in the main experiment. The predictions of fMRI time-series responses to the drifting bars were made by convoluting the product of a stimulus matrix and a two-dimensional isotropic Gaussian pRF model with the hemodynamic impulse response function parameterized by the differences of two gamma distribution functions (Glover 1999). The model parameters (x, y, and σ) were obtained by fitting the predicted time courses to the measured responses to four drifting directions (horizontal and vertical) for the initial guess, and finally determined by simultaneously fitting to the measured responses from the entire eight drifting directions. Unlike the retinotopic mapping procedure in the main experiment, the pRF locations were not assumed to be smooth over the cortical surface.

Stimulus tuning similarity estimation and resting-state measurements. For the SF tuning scans, the 14 non-overlapping bands of SF filters were modulated either in a monotonically increasing or decreasing manner throughout a given scan, unlike in the main experiment in which the filters were modulated in a cyclic manner. Six seconds (4 TRs) of a blank period was inserted at the end of each cycle (18 TRs total) to separate the responses to the lowest from those to the highest SF stimuli. Only the responses from the 3rd to 16th frames within each cycle were used for estimating SF tuning similarity. There were four (two increasing and two decreasing) SF scans and four (two CW and two CCW) OR scans. The resting-state scans and the "fixation with zero contrast" scans (432 s), both acquired twice for reliability, were inserted between the stimulus tuning scans.

Estimation of RF overlap. Having estimated the pRFs of individual voxels, we quantified the overlap between the pRFs of each voxel pair using the Hellinger distance (HD; Kailath 1967). The squared HD between two probability density functions P and Q are defined by

$$d^2_{\text{Hellinger}} = \frac{1}{2}\int \left(\sqrt{P} - \sqrt{Q}\right)^2.$$

Particularly, when P and Q are multivariate Gaussians (Pardo Llorente 2006),

$$d^2_{\text{Hellinger}} = 1 - \frac{|\Sigma_P|^{\frac{1}{4}}|\Sigma_Q|^{\frac{1}{4}}}{|\bar{\Sigma}|^{\frac{1}{2}}} \exp\left\{-\frac{1}{8}\left(\mu_P - \mu_Q\right)^T \bar{\Sigma}^{-1}\left(\mu_P - \mu_Q\right)\right\},$$

where Σ_P and Σ_Q are the covariance matrices, and μ_P and μ_Q are the mean vectors for the P and Q, respectively, and $\bar{\Sigma} = \left(\Sigma_P + \Sigma_Q\right)/2$. The HD takes the minimum value of 0 when the distributions of P and Q completely overlap, and approaches 1 as they become separated from each other. The sigma (σ) and mean (x, y) parameters of pRF were used for the covariance and mean terms, respectively, for $d_{\text{Hellinger}}$.

Voxel selection. Voxels were judged invalid and excluded for further analysis when the time series in the on-/off-stimulation, pRF mapping, and stimulus tuning scans exhibited any of the following: (i) when the mean variance in the on-/off-stimulation scans was within the highest 3% of the voxel population in a given area, (ii) when the goodness of fit (r-squared) of pRF estimation was less than 0.1, or when the estimated pRF center position fell outside the region of stimulation, (iii) when the SNR was within the lowest 70% in the stimulus tuning scans and within the lowest 30% in the on-/off-stimulation scan. In the ROIs,

12.2% of total voxels (213.8 ± 24.9 voxels per subject, mean ± s.e.m.) survived these criteria.

4.14. Statistical Test

To evaluate the differential contribution of the tuning similarity and distance factors to the variability in resting-state correlation, we conducted statistical analyses as follows. First, we ran a one-way repeated measures analysis of variance (ANOVA) to test whether significant differences existed over the factors of interest in terms of the mean level of explained variances (*r*-squared or squared part correlations). If this ANOVA returned a significant result, the Tukey-Kramer test was performed for *post hoc* evaluation of pairwise differences between the factors. When the comparison included the differences between visual areas, a two-way repeated measures ANOVA was conducted by adding the visual areas as a within-subject factor. The Sidak correction, with an alpha level of 0.05, was used to judge the significance of *post hoc* multiple comparisons, otherwise noticed.

Bibliography

Abbott LF, Dayan P. 1999. The effect of correlated variability on the accuracy of a population code. Neural Comput. 11:91–101.

Abdi H. 2007. Part and Partial Correlations. In: Salkind NJ editor. Encyclopedia of Measurement and Statistics. 2455 Teller Road, Thousand Oaks California 91320 United States of America: Sage Publications, Inc. p. 736–740.

Abrams J, Nizam A, Carrasco M. 2012. Isoeccentric locations are not equivalent: the extent of the vertical meridian asymmetry. Vision Res. 52:70–78.

Anderson JE, Leslie Cameron E, Levine MW. 2014. A method for quantifying visual field inhomogeneities. Vision Res.

Arcaro MJ, Honey CJ, Mruczek RE, Kastner S, Hasson U. 2015. Widespread correlation patterns of fMRI signal across visual cortex reflect eccentricity organization. eLife Sciences. 4:e03952.

Ashburner JT, Friston KJ. 1997. Multimodal image coregistration and partitioning—A unified framework. NeuroImage. 6:209–217.

Averbeck BB, Latham PE, Pouget A. 2006. Neural correlations, population coding and computation. Nat Rev Neurosci. 7:358–366.

Baldassarre A, Lewis CM, Committeri G, Snyder AZ, Romani GL, Corbetta M. 2012. Individual variability in functional connectivity predicts performance of a perceptual task. P Natl Acad Sci USA. 109:3516–3521.

Beck JM, Ma WJ, Pitkow X, Latham PE, Pouget A. 2012. Not noisy, just wrong: The role of suboptimal inference in behavioral variability. Neuron. 74:30–39.

Berens P. 2009. CircStat: a MATLAB toolbox for circular statistics. J Stat Softw. 31:1–21.

Berkes P, Orban G, Lengyel M, Fiser J. 2011. Spontaneous cortical activity reveals hallmarks of an optimal internal model of the environment. Science. 331:83–87.

Bianciardi M, Fukunaga M, van Gelderen P, Horovitz SG, de Zwart JA, Duyn JH. 2009. Modulation of spontaneous fMRI activity in human visual cortex by behavioral state. NeuroImage. 45:160–168.

Boly M, Balteau E, Schnakers C, Degueldre C, Moonen G, Luxen A, Phillips C, Peigneux P, Maquet P, Laureys S. 2007. Baseline brain activity fluctuations predict somatosensory perception in humans. P Natl Acad Sci USA. 104:12187–12192.

Bonhoeffer T, Grinvald A. 1991. Iso-orientation domains in cat visual

cortex are arranged in pinwheel-like patterns. Nature. 353:429–431.
Bosking WH, Zhang Y, Schofield B, Fitzpatrick D. 1997. Orientation selectivity and the arrangement of horizontal connections in tree shrew striate cortex. J Neurosci. 17:2112–2127.
Butt OH, Benson NC, Datta R, Aguirre GK. 2013. The fine-scale functional correlation of striate cortex in sighted and blind people. J Neurosci. 33:16209–16219.
Buzsáki G, Mizuseki K. 2014. The log-dynamic brain: How skewed distributions affect network operations. Nat Rev Neurosci. 15:264–278.
Canolty RT, Edwards E, Dalal SS, Soltani M, Nagarajan SS, Kirsch HE, Berger MS, Barbaro NM, Knight RT. 2006. High gamma power is phase-locked to theta oscillations in human neocortex. Science. 313:1626–1628.
Ch'ng YH, Reid RC. 2010. Cellular imaging of visual cortex reveals the spatial and functional organization of spontaneous activity. Front Integr Neurosci. 4:20.
Chan AW, Mohajerani MH, LeDue JM, Wang YT, Murphy TH. 2015. Mesoscale infraslow spontaneous membrane potential fluctuations recapitulate high-frequency activity cortical motifs. Nat Commun. 6:7738.
Chang C, Glover GH. 2010. Time–frequency dynamics of resting-state brain connectivity measured with fMRI. NeuroImage. 50:81–98.
Chen Y, Geisler WS, Seidemann E. 2006. Optimal decoding of correlated neural population responses in the primate visual cortex. Nat Neurosci. 9:1412–1420.
Choe KW, Blake R, Lee S-H. 2014. Dissociation between neural signatures of stimulus and choice in population activity of human V1 during perceptual decision-making. J Neurosci. 34:2725–2743.
Chu CCJ, Chien PF, Hung CP. 2014. Tuning dissimilarity explains short distance decline of spontaneous spike correlation in macaque V1. Vision Res. 96:113–132.
Chung MK, Hartley R, Dalton K, Davidson RJ. 2008. Encoding cortical surface by spherical harmonics. Statistica Sinica. 18:1269–1291.
Cordes D, Haughton VM, Arfanakis K, Carew JD, Turski PA, Moritz CH, Quigley MA, Meyerand ME. 2001. Frequencies contributing to functional connectivity in the cerebral cortex in "resting-state" data. Am J Neuroradiol. 22:1326–1333.
Dale AM, Fischl B, Sereno MI. 1999. Cortical surface-based analysis: I. Segmentation and surface reconstruction. NeuroImage. 9:179–194.
Das A, Gilbert CD. 1999. Topography of contextual modulations mediated by short-range interactions in primary visual cortex. Nature.

399:655–661.
DeAngelis GC, Ghose GM, Ohzawa I, Freeman RD. 1999. Functional micro-organization of primary visual cortex: receptive field analysis of nearby neurons. J Neurosci. 19:4046–4064.
Denman DJ, Contreras D. 2014. The structure of pairwise correlation in mouse primary visual cortex reveals functional organization in the absence of an orientation map. Cereb Cortex. 24:2707–2720.
Dijkstra EW. 1959. A note on two problems in connexion with graphs. Numerische Mathematik. 1:269–271.
Douglas RJ, Koch C, Mahowald M, Martin KAC, Suarez HH. 1995. Recurrent excitation in neocortical circuits. Science. 269:981–985.
Engel SA, Glover GH, Wandell BA. 1997. Retinotopic organization in human visual cortex and the spatial precision of functional MRI. Cereb Cortex. 7:181–192.
Estebanez L, Boustani SE, Destexhe A, Shulz DE. 2012. Correlated input reveals coexisting coding schemes in a sensory cortex. Nat Neurosci. 15:1691–1699.
Fisher RA. 1921. On the "Probable Error" of a coefficient of correlation deduced from a small sample. Metron. 1:3–32.
Fox MD, Snyder AZ, Vincent JL, Corbetta M, Van Essen DC, Raichle ME. 2005. The human brain is intrinsically organized into dynamic, anticorrelated functional networks. P Natl Acad Sci USA. 102:9673–9678.
Fox MD, Snyder AZ, Vincent JL, Raichle ME. 2007. Intrinsic fluctuations within cortical systems account for intertrial variability in human behavior. Neuron. 56:171–184.
Freeman J, Brouwer GJ, Heeger DJ, Merriam EP. 2011. Orientation decoding depends on maps, not columns. J Neurosci. 31:4792–4804.
Friston KJ, Williams S, Howard R, Frackowiak RSJ, Turner R. 1996. Movement-related effects in fMRI time-series. Magn Reson Med. 35:346–355.
Geisler WS, Perry JS, Super BJ, Gallogly DP. 2001. Edge co-occurrence in natural images predicts contour grouping performance. Vision Res. 41:711–724.
Gilbert CD, Wiesel TN. 1989. Columnar specificity of intrinsic horizontal and corticocortical connections in cat visual cortex. J Neurosci. 9:2432–2442.
Glickfeld LL, Andermann ML, Bonin V, Reid RC. 2013. Cortico-cortical projections in mouse visual cortex are functionally target specific. Nat Neurosci. 16:219–226.
Glover GH. 1999. Deconvolution of impulse response in event-related BOLD fMRI. NeuroImage. 9:416–429.

Gravel N, Harvey BM, Nordhjem B, Haak KV, Dumoulin SO, Renken R, Ćurčić-Blake B, Cornelissen FW. 2014. Cortical connective field estimates from resting state fMRI activity. Front Neurosci. 8:339.
Gray CM, König P, Engel AK, Singer W. 1989. Oscillatory responses in cat visual cortex exhibit inter-columnar synchronization which reflects global stimulus properties. Nature. 338:334–337.
Greschner M, Shlens J, Bakolitsa C, Field GD, Gauthier JL, Jepson LH, Sher A, Litke AM, Chichilnisky E-J. 2011. Correlated firing among major ganglion cell types in primate retina. J Physiol. 589:75–86.
Haefner RM, Gerwinn S, Macke JH, Bethge M. 2013. Inferring decoding strategies from choice probabilities in the presence of correlated variability. Nat Neurosci. 16:235–242.
He BJ, Snyder AZ, Zempel JM, Smyth MD, Raichle ME. 2008. Electrophysiological correlates of the brain's intrinsic large-scale functional architecture. P Natl Acad Sci USA. 105:16039–16044.
Heinzle J, Kahnt T, Haynes J-D. 2011. Topographically specific functional connectivity between visual field maps in the human brain. NeuroImage. 56:1426–1436.
Henriksson L, Nurminen L, Hyvärinen A, Vanni S. 2008. Spatial frequency tuning in human retinotopic visual areas. J Vision. 8:5–5.
Hess RF, Dakin SC. 1997. Absence of contour linking in peripheral vision. Nature. 390:602–604.
Hesselmann G, Kell CA, Eger E, Kleinschmidt A. 2008. Spontaneous local variations in ongoing neural activity bias perceptual decisions. P Natl Acad Sci USA. 105:10984–10989.
Huang X, Lisberger SG. 2009. Noise correlations in cortical area MT and their potential impact on trial-by-trial variation in the direction and speed of smooth-pursuit eye movements. J Neurophysiol. 101:3012–3030.
Hubel DH, Wiesel TN. 1962. Receptive fields, binocular interaction and functional architecture in the cat's visual cortex. J Physiol. 160:106–154.
Jermakowicz WJ, Chen X, Khaytin I, Bonds AB, Casagrande VA. 2009. Relationship between spontaneous and evoked spike-time correlations in primate visual cortex. J Neurophysiol. 101:2279–2289.
Kailath T. 1967. The divergence and Bhattacharyya distance measures in signal selection. IEEE Transactions on Communication Technology. 15:52–60.
Kara P, Boyd JD. 2009. A micro-architecture for binocular disparity and ocular dominance in visual cortex. Nature. 458:627–631.
Kiani R, Cueva CJ, Reppas JB, Peixoto D, Ryu SI, Newsome WT. 2015. Natural grouping of neural responses reveals spatially segregated

clusters in prearcuate cortex. Neuron. 85:1359–1373.
Ko H, Hofer SB, Pichler B, Buchanan KA, Sjöström PJ, Mrsic-Flogel TD. 2011. Functional specificity of local synaptic connections in neocortical networks. Nature. 473:87–91.
Kremkow J, Jin J, Wang Y, Alonso J-M. 2016. Principles underlying sensory map topography in primary visual cortex. Nature. 533:52–57.
Lakatos P, Karmos G, Mehta AD, Ulbert I, Schroeder CE. 2008. Entrainment of neuronal oscillations as a mechanism of attentional selection. Science. 320:110–113.
Lakatos P, Shah AS, Knuth KH, Ulbert I, Karmos G, Schroeder CE. 2005. An oscillatory hierarchy controlling neuronal excitability and stimulus processing in the auditory cortex. J Neurophysiol. 94:1904–1911.
Lee AT, Glover GH, Meyer CH. 1995. Discrimination of large venous vessels in time-course spiral blood-oxygen-level-dependent magnetic-resonance functional neuroimaging. Magn Reson Med. 33:745–754.
Lewis CM, Baldassarre A, Committeri G, Romani GL, Corbetta M. 2009. Learning sculpts the spontaneous activity of the resting human brain. P Natl Acad Sci USA. 106:17558–17563.
Liu T, Heeger DJ, Carrasco M. 2006. Neural correlates of the visual vertical meridian asymmetry. J Vision. 6:12–12.
Lu H, Zuo Y, Gu H, Waltz JA, Zhan W, Scholl CA, Rea W, Yang Y, Stein EA. 2007. Synchronized delta oscillations correlate with the resting-state functional MRI signal. P Natl Acad Sci USA. 104:18265–18269.
Malach R, Amir Y, Harel M, Grinvald A. 1993. Relationship between intrinsic connections and functional architecture revealed by optical imaging and in vivo targeted biocytin injections in primate striate cortex. P Natl Acad Sci USA. 90:10469–10473.
Maldonado PE, Friedman-Hill S, Gray CM. 2000. Dynamics of striate cortical activity in the alert macaque: II. Fast time scale synchronization. Cereb Cortex. 10:1117–1131.
Meister M. 1996. Multineuronal codes in retinal signaling. P Natl Acad Sci USA. 93:609–614.
Menon RS, Ogawa S, Tank DW, Uğurbil K. 1993. 4 Tesla gradient recalled echo characteristics of photic stimulation-induced signal changes in the human primary visual cortex. Magn Reson Med. 30:380–386.
Miller J-EK, Ayzenshtat I, Carrillo-Reid L, Yuste R. 2014. Visual stimuli recruit intrinsically generated cortical ensembles. P Natl Acad Sci USA. 111:E4053–E4061.
Mohajerani MH, Chan AW, Mohsenvand M, LeDue J, Liu R, McVea DA, Boyd JD, Wang YT, Reimers M, Murphy TH. 2013. Spontaneous cortical activity alternates between motifs defined by regional axonal

projections. Nat Neurosci. 16:1426–1435.
Monto S, Palva S, Voipio J, Palva JM. 2008. Very slow EEG fluctuations predict the dynamics of stimulus detection and oscillation amplitudes in humans. J Neurosci. 28:8268–8272.
Murphy K, Birn RM, Handwerker DA, Jones TB, Bandettini PA. 2009. The impact of global signal regression on resting state correlations: Are anti-correlated networks introduced? NeuroImage. 44:893–905.
Nassi JJ, Callaway EM. 2009. Parallel processing strategies of the primate visual system. Nat Rev Neurosci. 10:360–372.
Nauhaus I, Nielsen KJ, Disney AA, Callaway EM. 2012. Orthogonal micro-organization of orientation and spatial frequency in primate primary visual cortex. Nat Neurosci. 15:1683–1690.
Oliva A, Torralba A. 2001. Modeling the shape of the scene: A holistic representation of the spatial envelope. International Journal of Computer Vision. 1–31.
Olman CA, Inati S, Heeger DJ. 2007. The effect of large veins on spatial localization with GE BOLD at 3 T: Displacement, not blurring. NeuroImage. 34:1126–1135.
Palva JM, Palva S. 2012. Infra-slow fluctuations in electrophysiological recordings, blood-oxygenation-level-dependent signals, and psychophysical time series. NeuroImage. 62:2201–2211.
Pardo Llorente L. 2006. Divergence Measures: Definition and Properties. In: Statistical inference based on divergence measures. Boca Raton, FL: Chapman & Hall/CRC. p. 1–53.
Park SH, Cha K, Lee S-H. 2013. Coaxial anisotropy of cortical point spread in human visual areas. J Neurosci. 33:1143–1156.
Radicchi F. 2014. Driving interconnected networks to supercriticality. Phys Rev X. 4:021014.
Raemaekers M, Schellekens W, van Wezel RJA, Petridou N, Kristo G, Ramsey NF. 2014. Patterns of resting state connectivity in human primary visual cortical areas: a 7T fMRI study. NeuroImage. 84:911–921.
Ringach DL. 2009. Spontaneous and driven cortical activity: Implications for computation. Curr Opin Neurobiol. 19:439–444.
Roe AW, Ts'o DY. 1999. Specificity of color connectivity between primate V1 and V2. J Neurophysiol. 82:2719–2730.
Romano SA, Pietri T, Pérez-Schuster V, Jouary A, Haudrechy M, Sumbre G. 2015. Spontaneous neuronal network dynamics reveal circuit's functional adaptations for behavior. Neuron. 85:1070–1085.
Schölvinck ML, Friston KJ, Rees G. 2011. The influence of spontaneous activity on stimulus processing in primary visual cortex. NeuroImage. 59:2700–2708.

Schölvinck ML, Maier A, Ye FQ, Duyn JH, Leopold DA. 2010. Neural basis of global resting-state fMRI activity. P Natl Acad Sci USA. 107:10238–10243.
Schulz DPA, Sahani M, Carandini M. 2015. Five key factors determining pairwise correlations in visual cortex. J Neurophysiol. 114:1022–1033.
Shmuel A, Yacoub E, Chaimow D, Logothetis NK, Uğurbil K. 2007. Spatio-temporal point-spread function of fMRI signal in human gray matter at 7 Tesla. NeuroImage. 35:539–552.
Sigman M, Cecchi GA, Gilbert CD, Magnasco MO. 2001. On a common circle: Natural scenes and Gestalt rules. P Natl Acad Sci USA. 98:1935–1940.
Simoncelli EP, Olshausen BA. 2001. Natural image statistics and neural representation. Annu Rev Neurosci. 24:1193–1216.
Sincich LC, Blasdel GG. 2001. Oriented axon projections in primary visual cortex of the monkey. J Neurosci. 21:4416–4426.
Smith MA, Kohn A. 2008. Spatial and temporal scales of neuronal correlation in primary visual cortex. J Neurosci. 28:12591–12603.
Snyder AC, Morais MJ, Willis CM, Smith MA. 2015. Global network influences on local functional connectivity. Nat Neurosci. 18:736–743.
Sporns O. 2010. Networks of the Brain. MIT Press.
Stettler DD, Das A, Bennett J, Gilbert CD. 2002. Lateral connectivity and contextual interactions in macaque primary visual cortex. Neuron. 36:739–750.
Stevens WD, Buckner RL, Schacter DL. 2010. Correlated low-frequency BOLD fluctuations in the resting human brain are modulated by recent experience in category-preferential visual regions. Cereb Cortex. 20:1997–2006.
Thesen S, Heid O, Mueller E, Schad LR. 2000. Prospective acquisition correction for head motion with image-based tracking for real-time fMRI. Magn Reson Med. 44:457–465.
Tootell RBH, Switkes E, Silverman MS, Hamilton SL. 1988. Functional anatomy of macaque striate cortex. II. Retinotopic organization. J Neurosci. 8:1531–1568.
Ts'o DY, Gilbert CD, Wiesel TN. 1986. Relationships between horizontal interactions and functional architecture in cat striate cortex as revealed by cross-correlation analysis. J Neurosci. 6:1160–1170.
van den Heuvel MP, Sporns O. 2011. Rich-club organization of the human connectome. J Neurosci. 31:15775–15786.
Vanhatalo S, Voipio J, Kaila K. 2005. Infraslow EEG activity. In: Electroencephalography: Basic principles, clinical applications, and related fields. 5 ed. Philadelphia: Lippincott Williams and Wilkins. p.

489–493.
Yeo BTT, Krienen FM, Sepulcre J, Sabuncu MR, Lashkari D, Hollinshead M, Roffman JL, Smoller JW, Zollei L, Polimeni JR, Fischl B, Liu H, Buckner RL. 2011. The organization of the human cerebral cortex estimated by intrinsic functional connectivity. J Neurophysiol. 106:1125–1165.
Zohary E, Shadlen MN, Newsome WT. 1994. Correlated neuronal discharge rate and its implications for psychophysical performance. Nature. 370:140–143.

국문초록

인간 시각영역내 상관된 대뇌활동의 기능구조

서울대학교 대학원

자연과학대학 뇌인지과학과

류 중 원

대뇌 피질은 뉴런들 간의 긴밀한 연결로 구성된 대단위 네트워크이다. 감각 처리 시스템에서, 감각기관과 감각 피질 영역들, 그리고 감각 피질 내의 뉴런들은 각기 계층적 혹은 수평적 연결을 통해 연결되어있다. 흥미롭게도, 이렇게 복잡하게 연결된 네트워크에서는 특정 영역에서 발생한 국지적 신경활동들은 인접 영역에 영향을 미치게 되어 상관관계가 발생하게 된다. 이러한 상관된 뉴런들의

집단적 활동은 감각 표상 측면에서 매우 중요하므로, 외부 자극이 없이 다양한 시공간 스케일에서 자발적으로 발생하는 신경활동에 대한 연구가 진행되어왔다. 본 연구에서는 기능성 자기공명 영상법을 사용하여 인간 초기 시각피질의 대규모 집단적 신경활동에 존재하는 상관관계의 구조를 연구하였다. 구체적으로, 이미 기존 연구를 통해 알려져 있는 뉴런들 간의 편향된 해부학적 연결 패턴에 착안하여, 시각영역 각 회백질 위치쌍들을 (i) 시각장에서 정의된 수용장들 간의 거리, (ii) 대뇌 피질 표면을 따라 정의된 피질 거리, 그리고 (iii) 공간주파수와 방위 자극에 대한 반응의 유사도(조율 유사도)로 특성화하고, 이 세 요인들이 상관된 기능적 자기공명 영상 신호에 기여하는 정도를 서로 분리하여 평가 및 비교하였다. 그 결과 각 요인들 마다 고유한 설명 변량이 존재함을 확인하였으며, 그 중에서 자극에 대한 조율의 유사도가 거리 요인들보다 훨씬 큰 기여도를 보였다. 거리 요인에 대한 조율 유사도의 기여도의 우위는 V1, V2, V3 의 각 영역 내에서, 그리고 이 영역들 사이에서 시각 자극의 제시 여부나 자극의 세기와 무관하게 일관적으로 발견되었다. 이외에도, 자극의 특징에 조율된 상관구조가 시각장내의 각위치와 이심률에따라 체계적으로 달라짐을 관찰하였다. 또, 자발적인 기능적 자기공명 영상 활성의 공변산은 시간에따라 변화하며, 이러한 다이나믹스는 조율

유사도와 거리 요인에 의하여 지배됨을 발견하였다. 이는 인간 초기 시각 피질의 자발적 신경 활동은 거리나 기능 등 서로 다른 요인에 의해 중층적으로 정의된 네트워크에서 발생하는 국지적 영역들 사이의 상호작용으로 이해될 수 있음을 보여준다. 본 연구는, 거리 요인보다 조율 유사도 요인에 의해 지배되는 층이 시각 피질 네트워크에 훨씬 지배적 영향을 미친다는 것을 보여준다.

주요어: 자발 활동, 공변산 구조, 휴지상태, 기능적 연결성, 자극조율, 시각피질, 대뇌 진행파, 기능성 자기공명 영상법, 피질 거리

학 번: 2010-30767